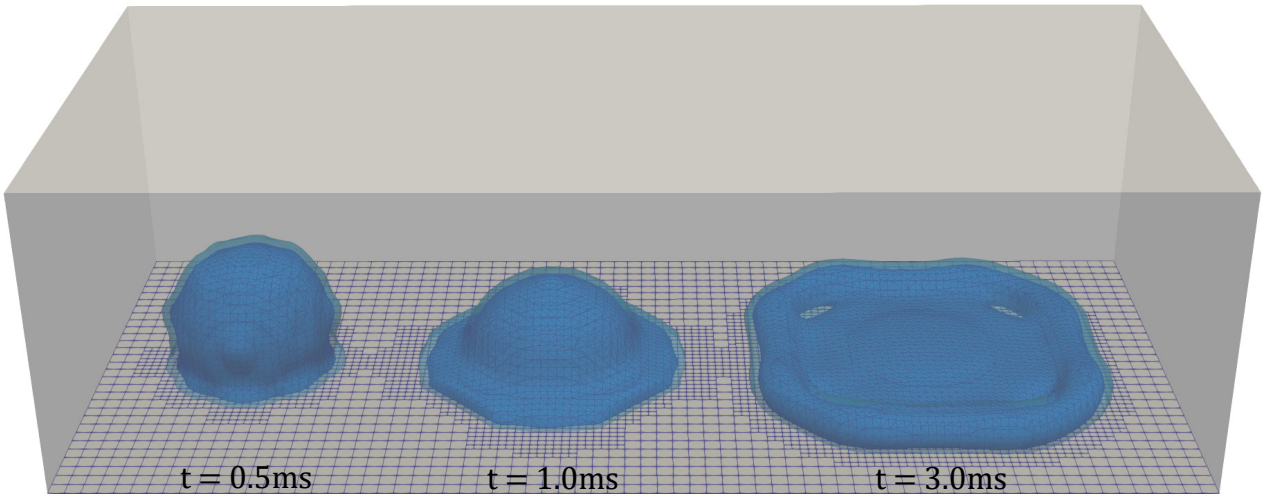

Multiphase CFD simulation of a packed bed scrubber using periodic boundary conditions

Andreas Krogh

Energy Technology, TEPE4-1007, 2020-06

Master's Thesis

MATLAB R2019a, Inkscape 0.92.2, Overleaf v2, OpenFOAMv6, OpenFOAMv1906, ParaView, Ansys Fluent

Energy Technology
Aalborg University
http://www.aau.dk

AALBORG UNIVERSITY
STUDENT REPORT

Title:
Multiphase CFD simulation of a packed bed scrubber using periodic boundary conditions

Theme:
Numerical flow simulations

Project Period:
Spring 2020

Project Group:
TEPE4-1007

Participant(s):
Andreas Krogh

Supervisor(s):
Kim Sørensen
Thomas Condra
Anders Schou Simonsen

Page Numbers: 72

Date of Completion:
29th of May 2020

Abstract:

In this study a numerical analysis of the flow behaviour on and around filling elements in an exhaust gas scrubber is conducted using the Volume of Fluid method and periodic boundary conditions. Two VOF models have been tested with the difference being the schemes, MULES or isoAdvector, used to recreate the interphase between the fluids. The specific pressure loss and water droplets terminal velocity have been validated using periodic boundaries. Furthermore simulations of the dynamic behaviour of water droplets on solid surfaces have been conducted and validated against empirical data. The simulations of the water and gas behaviour around the filling elements showed that the MULES scheme requires a fine mesh to properly resolve the interphase. On the other hand the isoAdvector scheme was able to obtain a sharp interphase on a coarser mesh, however the water volume within the system was not conserved over time.

Executive summary

The focus on the ambient air quality have been increasing over the past years and for the marine industry this has led regulations regarding the emissions of SO_x. As of 2020 the emission of SO_x should not exceed 0.5% globally and 0.1% in certain areas close to coastlines and harbours.[IMO, 2018]. One way of complying with these regulations is to install a sea water scrubber on the individual vessels that removes the sulphur content from the exhaust gas by scrubbing with water. In this study Computational Fluid Dynamics (CFD) is used to to predict the flow behaviour and performance of the packed bed absorption column in a scrubber in terms of specific pressure loss and interfacial area. The computational domain is only a small section of the entire column and periodic boundary conditions were utilized. Two two-phase Volume of Fluid models, **interCyclicFoam** and **interIsoCyclicFoam**, were developed with the difference between them being the scheme used to recreate the interphase between the fluids.

Two different validations were conducted to investigate the performance of using periodic boundary conditions. The first was of the pressure loss in a duct of a single phase, where the results form a transient simulations on a small domain using periodic boundary conditions were compared to a steady state simulation of a full size duct and an analytical solution. The second was of the terminal velocity of a water droplet. Simulations were made using both solvers on a small domain with periodic boundary conditions. The results were compared to an analytical solution that uses the force balance of the water droplet to predict the terminal velocity.

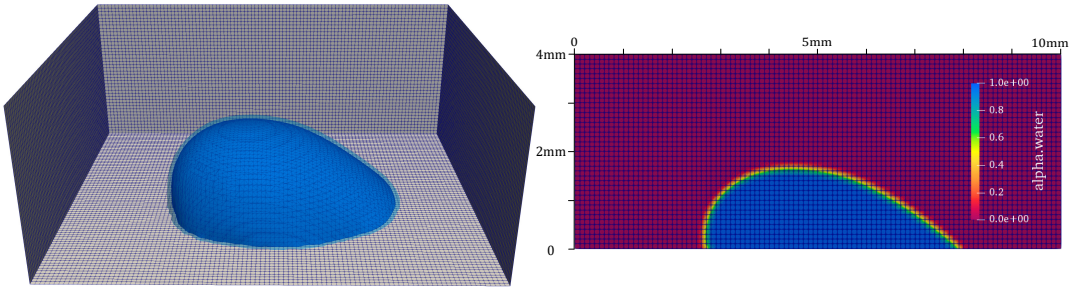

Figure 1: Dynamic droplet behaviour on inclined solid surface.

The absorption column of a scrubber is filled with filling elements and it is important that the model can accurately predict the fluid dynamics occurring when the water interacts with the filling elements. First a series of simulations for different wettability characteristics of the solid surface were conducted. These showed that a high wettability of the solid surface leads to the droplet occupying a large area on the surface which leads to a thin film layer. Further more it was shown that the shape of a

water droplet at rest on a solid surface can be considered as a spherical cap at Bo < 1. Next the dynamic behaviour of water droplets vertically hitting a solid surface were investigated. Two simulations were conducted with a 2mm diameter droplet and impact velocity 0.5m/s and 1m/s. The maximum spreading diameter were well in the range of empirical correlations from other studies. Finally the dynamic behaviour of water droplets moving alongside an inclined solid surface is investigated for varying droplet size and inclination angle. In Figure 1 the steady droplet shape is shown for a 25µL droplet on a 60° inclined surface.

The performance of the two solvers were tested on a simplified geometry of a small section from an absorption column as shown in Figure 2a. The initial state has 24 water droplets positioned evenly within the domain which corresponds to 3% of the entire volume. Simulations were conducted on three mesh refinements, 448 000 cells, 1 512 000 cells and 3 584 000 cells, to investigate how the models accuracy scaled with mesh refinement. In Figure 2b the results after 0.5s is shown when using the **interCyclicFoam** solver and the fine mesh with 3 584 000 cells. Based on the simulations it can be concluded that the **interIsoCyclicFoam** solver does obtain a sharp interphase between the fluid phases even for coarse meshes, however the model does not conserved the water volume over time. The **interCyclicFoam** solver on the other hand did conserved the water volume, but a much finer grid in required to obtain a sharp interphase between the fluid phases.

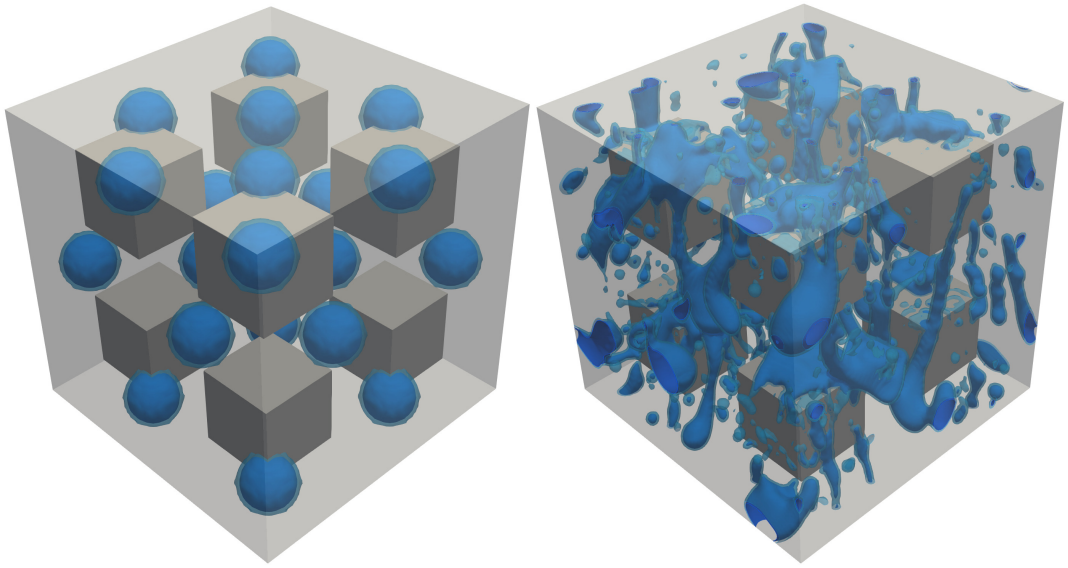

(a) Initial state. **(b)** $t = 0.5$s

Figure 2: Fill simulations results using the **interCyclicFoam** solver.

Preface

This Master's Thesis is written by energy engineering student Andreas Krogh from Aalborg University in the period from the 3th of February 2020 to the 29th of May 2020. This report concludes the 4th semester of the M.Sc in Thermal Energy and Process Engineering at the department of Energy Technology. The project has been carried out with the guidance of Kim Sørensen, Associate Professor, Aalborg University, Thomas Condra, Associate Professor, Aalborg University and Anders Schou Simonsen, Alfa Laval, Aalborg.

Reading instructions

The report makes use of references according to the Harvard method. The references will occur in the text in the following manner: [Surname/publisher, year (possible page number)], where the end of the report is a comprehensive list of literature.

Reference numbers are made as hyperlinks in the digital copy. Figures and tables are listed as the chapter number, followed by the figure/table/equation number, as an example Figure 7.2 is the second figure in Chapter 7. Figure and table explanatory text can be found below the figure and above tables. Furthermore, section references are made using the section numbering. The unit system used in the report is the SI system with a dot as decimal separator.

Aalborg University, 29th of May 2020

Nomenclature

Symbols

a	Acceleration	$\mathrm{m^2\,s^{-1}}$
C_D	Drag coefficient	–
D	Diameter	m
dp	Pressure gradient	$\mathrm{Pa\,m^{-1}}$
F	Force	N
f	Friction Factor	–
$f_{\sigma\,\mathrm{i}}$	Surface tension	$\mathrm{N\,m^{-1}}$
g	Gravitational Acceleration	$\mathrm{m\,s^{-2}}$
h	Height	m
L_{h}	Entry Length	m
P	Pressure	Pa
R	Contact area radius	m
r	Radius	m
t	Time	s
U	Velocity	$\mathrm{m\,s^{-1}}$
V	Volume	$\mathrm{m^3}$
x	Length	m

Greek Symbols

α	Inclination angle	$^\circ$
α_{water}	Liquid volumetric fraction	–
β_{max}	Maximum spreading factor	–
ϵ	Surface Roughness	m
γ	Interfacial tension	$\mathrm{N\,m^{-1}}$
λ	Capillary length	m

μ	Dynamic viscosity	$\mathrm{kg\,m^{-1}\,s^{-1}}$
ρ	Density	$\mathrm{kg\,m^{-3}}$
σ	Surface Tension	$\mathrm{N\,m^{-1}}$
τ	Viscous stress	Pa
τ_t	Turbulent stress	Pa
θ	Contact angle	$^\circ$

Subscripts

0	Impact values
a	Advancing
a	Air
avg	Average
b	Buoyancy force
D	Drag force
d	Droplet
g	Gas
g	Gravitational force
l	Liquid
lg	solid-gas
r	Receding
rgh	Hydrostatic pressure effects
s	Source term
sg	solid-gas
sl	solid-liquid
w	Water

Dimensionless Groups

Bo	Bond Number
MN	Merve Number

Re	Reynolds Number
We	Weber Number

Abbreviations

CFD	Computational Fluid Dynamics
IMO	International Maritime Organization
VOF	Volume of Fluid
WHO	The World Health Organisation

Contents

1 Introduction

Air pollution is one of the largest enviormental risk to human health according to The World Health Organisation WHO who estimates that a total of 4.2 million deaths every year is caused by ambient air pollution [WHO, 2016]. Over the years several regulations regarding emissions have been made as an attempt to improve the ambient air quality. In the marine industry, which is the focus of this study, the regulations are made by the International Marine Organization (IMO). They formulated a set of regulations stating that the emissions of SO_x should not exceed 0.5% globally and 0.1% in certain areas close to coastlines and harbours [IMO, 2018]. One way of complying with these regulations is to install a sea water scrubber on the individual vessels. The scrubber removes the sulphur content from the exhaust gas by scrubbing with water. This project is made in corporation with Alfa Laval Aalborg who is both a developer and manufacture of sea water scrubbers..

In the marine industry, and industry in general, Computational Fluid Dynamics (CFD) has gained increasingly popularity over the years as a tool to predict and improve the performance of designs, where full scale testing or even model-scale testing is both expensive and time consuming. The advantages of using CFD as a supplement to tests is that the configuration easily can be changed and parametric studies can be performed. This is often required in complex cases to obtain an optimum in performance. The reason CFD is gaining more and more popularity is the still increasing computational power that allows more and more accurate model results within a reasonable time frame.
From a numerical perspective one of the greatest challenges with CFD is to accurately describe the interphase between two phases in multiphase simulations [Roenby J, 2017]. This is a problem often encountered in the marine industry where the combination of water and air or gas is common. A prominent example of this is the absorption column of an offshore sea water scrubber where the two fluids exhaust gas and water are interacting and this, as mentioned above, is the underlying focus of this project. A number of different scrubber designs exist, but the most common is the U-shaped scrubber, a sketch of such a scrubber is shown in Figure 1.1.

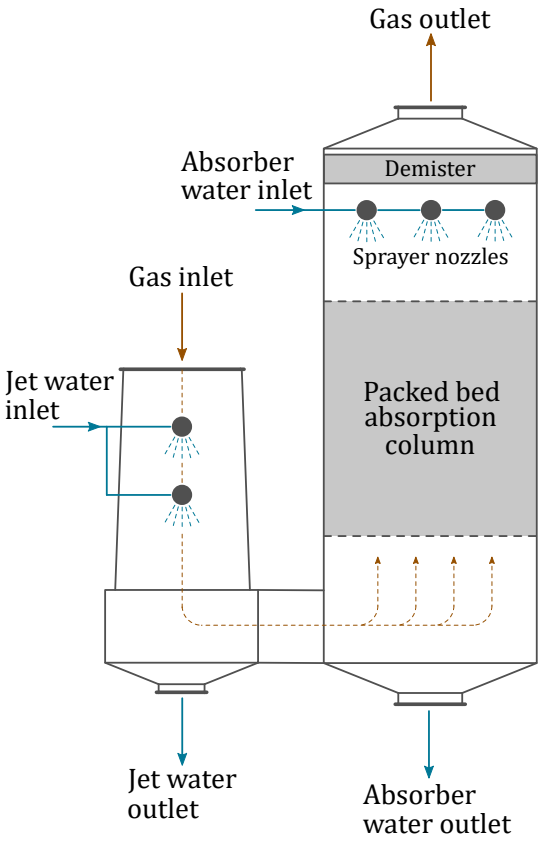

Figure 1.1: A sketch of the U-shaped scrubber. The left hand side of the sketch is the jet and the right hand side in the absorber.[Simonsen, 2018]

The exhaust, which comes form the ships main engine, that has to be cleaned for SO_x and other particulate matter, enters the scrubber in the jet section, the left part in Figure 1.1. In the jet section the exhaust gas is quenched by the cocurrent water sprayers where a small part of the sulphur content is removed. The exhaust gas then enters the bottom of the absorption column which is filled with filling elements in order to increase the interfacial area between water and gas, an example of such an element is shown in Figure 1.2. The flow distribution of the gas will be even over the cross sectional area of the column due to the pressure loss provided by both the filling elements and the water. The water is injected through a number of evenly distributed sprayers at the top of the column. It then passes through the filling elements and the gas before exiting at the bottom of the column.
In 2019 Alfa Laval has sold more that 500 scrubbers world wide with total of 1.9 million operating hours. 54% of them were installed in new vessels whereas 46% were retrofit projects. The operation of a scrubber unit on board a typical merchant ship involves the movement of approximately $950 m^3/h$ and with a pumping height of 20 meters this requires a pumping capacity of 58kW. Furthermore the scrubber installation gives an increase in the exhaust gas back-pressure on the main engine

which reduces the engine efficiency, though by a small amount. These considerations are important design parameters for a scrubber unit and which can give basis for the use of considerable resources in the development and design phases of such a scrubber unit. Most scrubbers are designed for the individual vessels, but the scale of a typical sea water scrubber is approximately 3m high and with a diameter of 4.5m.
[Laval, 2019]

1.1 Filling Elements

As the focus in this project is on the fluid behaviour inside the absorption column the filling elements is of great interest. The purpose of the filling elements is to increase the interfacial area between water and the exhaust gas. This is primarily achieved by a thin film layer that surrounds all the filling elements when the scrubber is operating. In Figure 1.2 an example of a single filling element used in a sea water scrubber is shown.

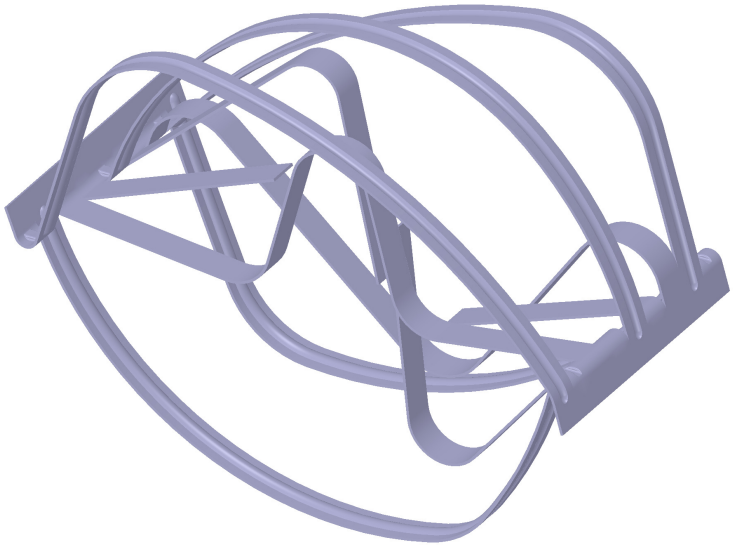

Figure 1.2: An example of a filling element used in the absorption column in a U-shaped sea water scrubber.

The size of such a filling element is in the range 90x70x50 mm, however the important parameter is the surface area which is 12.400 mm^2. With approximately 4400 filling elements per cubic meter this gives a specific surface area of 54.5 m^2/m^3.

1.2 Objective

The focus of this study is the water-gas interaction in the absorption column. The outer geometry of the scrubber is a simple cylinder, but the inside is very complex

due to the presence of the filling elements. Numerically solving the entire volume of the scrubber would require a lot more computational power than is available. The problem requires a two-phase solver (water and gas), where the interphase between the two phases is of interest and has to be resolved sufficiently to obtain an accurate solution. This is computationally very expensive and as a result this project only investigates a small section of the packed bed column containing a few filling elements. The assumptions for the small section is that it is sufficiently far away from both the internal walls, inlet and outlet, for them to have an impact on the flow in the computational domain. This allows the use of periodic boundary conditions where the field values for pressure, velocity and water volumetric fraction at the bottom of the domain are copied to the top at every time step and similarly from the left to the right side and front to back, this will be explained in more details in Chapter 2. Other assumptions is that there is no heat transfer between the fluids and both of them be can be considered incompressible.

This study seeks to develop a model capable of solving two-phase flow with the phases in counterflow and periodic boundary conditions on all sides. The validation of the model includes specific pressure loss, water volume conservation and terminal velocities of water droplets. The development of the model is described in Chapter 2 and validation of the specific pressure loss and droplet terminal velocity are presented in Chapter 3. Two important parameters that the model should be able to predict are the specific pressure loss and the specific interfacial surface area between the two phases. The pressure loss is an important parameter in the design of a scrubber and will increase with increasing gas velocity, a higher amount of water in the system and the compactness of the filling elements. The specific interfacial surface area is the critical factor in the removal of sulphur from the exhaust gas. It is important that the area is large enough to remove all the sulphur content in the gas.

This study also investigates the flow behaviour of water droplets interaction with solid surfaces. In the scrubber all the filling elements are considered solid surfaces and it is important that the model can accurately predict the flow dynamics when water interacts with these surfaces. Under operation it is assumed that all the filling elements is the absorption column are covered by a thin film layer of water which gives the high interfacial area between the gas and liquid. The development and properties of this film layer depends of the wettability characteristics of the solid surface and the physical properties of the liquid. The study of waters interaction with solid surfaces is separated into three parts. The first, Section 4.1, investigates the geometry of a water droplet at its equilibrium state on a solid surface and how it changes with different wettability of the solid and droplet properties. This is expanded in Section 4.2 where the transient behaviour of a water droplet hitting a solid surface with varying impact velocity is investigated. Finally the dynamic behaviour of a water droplet on an inclined surface is investigated in Section 4.3. Similarly to the model described in Chapter 3 this utilizes a small domain with periodic boundary conditions. Com-

mon for the entire Chapter 4 is that all the CFD simulation results are compared and validated against analytical solution and/or experimental work found in other studies.

Finally the models described in Chapter 2 are used on a small simplified scrubber section in Chapter 5 with a simplified geometry of the filling elements compared to Figure 1.2 to improve the stability of the models. The chapter investigates the specific interfacial area between the two phases and the conservation of the water volume over time. The simulations are conducted of three different mesh refinements to investigate how the performance for both solvers scale with mesh refinement.

1.3 State of the art

This section present studies made with the overall focus on the performance of a scrubber and parameters effecting it. Throughout the project validations will be done where the simulation results are compared to state of the art from other studies and these will be presented under the respective sections.

Some previous studies have also analyzed the performance of a scrubber using various computational methods. Reference Ali Majid [2012] modelled a venturi scrubber using the commercial software Ansys CFX. The focus in the study was on dust removal and the simulations used a three phase Eulerian-Lagrangian model. The dust removal efficiency was found to increase with increasing liquid and gas flow rates.

A similarly study by Manisha Bal [2017] used a Volume of Fluid model in Ansys to study the performance of a venturi scrubber. The study had a higher focus on the hydrodynamics and used the simulations to predict the pressure loss profile inside the venturi scrubber. Three parameters were found that increased the pressure loss which was a higher gas velocity, higher liquid mass flow rate and higher liquid to gas ratio.
Both of these studies is of a venturi scrubber where the liquid and gas are in cocurrent flow. In the U-shaped scrubber, which is of interest in this study, this is not the case as the liquid and gas are in countercurrent. However the pressure loss dependency of gas velocity, liquid mass flow rate and liquid to gas ratio are expected to have a similar trend to the cocurrent studies.

In reference Ion Iliuta [2019] simulations using the commercial software Aspen have been performed to predict the performance of three different packings in a packed bed absorption column. The model is an Eulerian 3-D model that uses the macroscopic volume-averaged continuity, momentum, species and energy balance equations for the liquid and gas phase. Significant differences in the pressure loss were found for the different packings. When looking at the scrubbing process it was found that a higher liquid flow rate and lower liquid temperature where the dominant parameters to enhance the process.

Reference Andraž Pavlišič [2018] used a laminar steady-state incompressible solver available within OpenFOAM to model the flow around four simple filling elements. A series of empirical correlations were used to validate the pressure loss caused by the filling elements. It was found that there was a good agreement between the empirical correlations and the simulations results when inside the validity range for the correlations. These simulations were only of a single fluid phase and are thereby not directly applicable to absorption column as it contains both liquid and gas.

2 | Solver

For multiphase simulations two overall methods are available and the choice depends on the application. The first is the Euler-Lagrange approach where the fluid phase is treated as a continuum by solving the Navier Stokes equations and the dispersed phase is solved by tracking a number of particles. However in this project the interphase between the two fluids is of interest and the Euler-Lagrange approach is therefore not applicable.
Instead an Euler-Euler model is utilized which treats the interphase as interpenetrating continua. The widely used Euler-Euler surface tracking model is the Volume of Fluid (VOF) model. In the following chapter the implementation of the VOF model in OpenFOAM is described as well as a discussion of surface representation which is of great importance if valid results are to be obtained.

2.1 Volume of Fluid

The VOF method was first presented by Nichols [1979]. It uses an indicator function of the water volumetric fraction α_{water} to determine the position of the interphase between the two fluids. A value of zero corresponds to the first fluid, in this project the gas, and a value of one corresponds to the second fluid or the water is the project. This indicator function is calculated for all cells in the domain and the interphase between the two fluids is located in the cells with $0 < \alpha_{\text{water}} < 1$. This is illustrated in Figure 2.1. [OpenFOAMWiki, 2018].

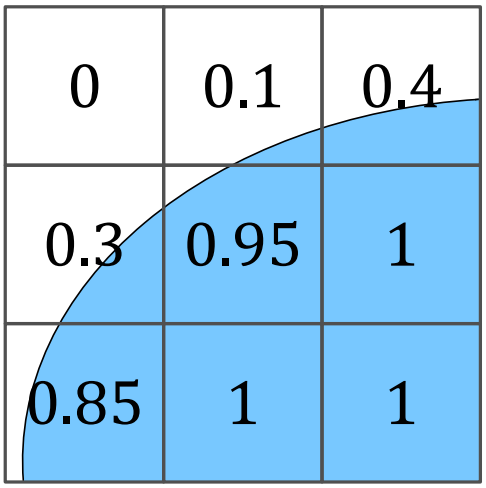

Figure 2.1: The principle of the VOF model shown on a 3x3 mesh. The numbers is the liquid volumetric fraction.

The VOF method solves the continuity and momentum equations, shown in Equation 2.1 and 2.3, alongside the transport equation for the indicator function, shown in Equation 2.2.

$$\nabla \cdot U = 0 \tag{2.1}$$

$$\frac{\partial \alpha}{\partial t} + \nabla \cdot (U\,\alpha) = 0 \tag{2.2}$$

$$\frac{\partial (\rho\, u_{\mathrm{i}})}{\partial t} + \nabla \cdot (\rho\, u_{\mathrm{j}}\, u_{\mathrm{i}}) = -\nabla p + \nabla \cdot (\tau_{\mathrm{ij}} + \tau_{\mathrm{t_{ij}}}) + \rho\, g_{\mathrm{i}} + f_{\sigma \mathrm{i}} \tag{2.3}$$

Here U is the velocity, α is the volumetric fraction of the liquid, ρ is the density, p is the pressure, τ_{ij} and $\tau_{\mathrm{t_{ij}}}$ is the viscous and turbulent stresses and $f_{\sigma \mathrm{i}}$ is the surface tension. It should be noted that while the indicator function ensures mass conservation in the system it does not reconstruct a smooth interphase which which leads to difficulties in the calculation of interphase properties such as surface tension. In this project the surface tension is assumed to be constant and for pure fluids, however more detailed models to handle the surface tension exist as described in M.W. Baltussen [2014], who investigated the performance of three different methods for handling surface tension in VOF simulations.

The addition of the indicator function α_{water} in the VOF method reduces the number of equations required compared to other multiphase models as the velocity- and pressure field is shared by both phases. The physical properties, density and viscosity, are approximated as weighted averages based on α_{water} in the cell as shown in Equation 2.4 and 2.5. The physical properties will only vary in the interphase where cells contains a mixture of water and gas.

$$\rho = \rho_{\mathrm{l}}\, \alpha + \rho_{\mathrm{g}}\, (1 - \alpha) \tag{2.4}$$

$$\mu = \mu_{\mathrm{l}}\, \alpha + \mu_{\mathrm{g}}\, (1 - \alpha) \tag{2.5}$$

2.1.1 InterFoam

The simulations are carried out using the software OpenFOAM which is an abbreviation for *Open-source Field Operation And Manipulation*. It allows the implementation of customized solvers, boundary conditions etc. and is written in C++. The model chosen for this project is the interFoam solver which it available in OpenFOAM. It is a solver for two incompressible, isothermal immiscible fluids using the VOF method. The assumption that the fluids are incompressible and isothermal are deemed valid as the changes in pressure and temperature are negligible in the small section of the absorption column. For the purpose of this study some adjustment have been made to the interFoam solver, this will be discussed further in Section 2.3. [OpenFOAMWiki, 2018]

2.2 Surface Representation

In the ideal case the interphase between the two phases is a discontinuous jump from $\alpha_{\text{water}} = 1$ to $\alpha_{\text{water}} = 0$. This is however not possible to obtain in CFD simulations and the interphase will instead be smeared over a few cells where the α_{water} gradually changes from 1 to 0. Since the introduction of the VOF method a number of schemes have been developed to improve the surface resolution. When the cells that contain the interphase are determined the challenge lies in determining where the cells are cut by the water surface. The interFoam solver utilizes a scheme called MULES to improve surface sharpness. A modified version of the interFoam solver called interIsoFoam were recently developed by Roenby J [2016] to further improve the sharpness. Instead of the MULES scheme it utilizes a method called isoAdvector. The model were developed for wave simulations. In this project the performance of both the original interFoam and the new interIsoFoam are investigated on water droplets in gas.

2.3 Cyclic interFoam/interIsoFoam

In the formulation of both interFoam and interIsoFoam the hydrostatic pressure is lumped into the pressure and this alternative pressure term is used in the momentum equation. This is shown in Equation 2.6 and is called p_{rgh} in OpenFOAM. The alternative momentum equation which is implemented in the interFoam and interIsoFoam solvers is shown in Equation 2.7. This is often used in buoyant and multiphase cases where it is numerically convenient to use this alternative pressure definition.

$$p_{\text{rgh}} = p + \rho(g\,h) \tag{2.6}$$

$$\frac{\partial(\rho\,u_{\text{i}})}{\partial t} + \nabla\cdot(\rho\,u_{\text{j}}\,u_{\text{i}}) = -\nabla p_{\text{rgh}} + \nabla\cdot(\tau_{\text{ij}} + \tau_{\text{t}_{\text{ij}}}) + f_{\sigma\text{i}} \tag{2.7}$$

However when using periodic boundary conditions the pressure field is not copied correctly from one patch to the other due to the hydrostatic part being lumped into the pressure term. This results in a nonphysical solution where the water volume is not conserved over the periodic boundaries. To circumvent this problem both interFoam and interIsoFoam have been rewritten to separate the hydrostatic part from the pressure term. Equation 2.6 is rewritten to Equation 2.8 and substituted into Equation 2.7 which results in the momentum eqaution as presented in Section 2.1.

$$\nabla p_{\text{rgh}} = -\nabla p + \rho\,g + \underbrace{g\,h\,\nabla\rho}_{0} \tag{2.8}$$

Here the last term is zero as the solver is for incompressible fluids. The updated models will be referred to as **interCyclicFoam** and **interIsoCyclicFoam** with the only difference between them being the scheme used to improve interphase sharpness.

2.4 Velocity Control

As mentioned previously the water and exhaust gas are in counterflow to each other in the absorption column. The water will naturally fall down due to gravitational forces, but the gas requires some additional force to move in the upwards direction. As the simulation are done on a small section of the column with periodic boundary conditions in inlet and outlet the velocity field can not be controlled in the boundary. Instead the velocity of the gas is controlled by a source term added directly to the momentum equation at every time step. It is done using the function *meanVelocity-Force* within OpenFOAM. This function allows the user to specify an average velocity field as a vector for the entire computational domain, $\bar{U} = (\bar{U}_x\, \bar{U}_y\, \bar{U}_z)$. At every time step the model then calculates the source term required to fulfill the desired average velocity field. An example where the *meanVelocityForce* is set to $\bar{U} = (0\,3\,0)$, with the y-direction being opposite to the gravitational force, then the model would calculate a source term that fulfils this criteria at every time step. However it is important to emphasise that an $\bar{U} = (0\,3\,0)$ is not equal to a gas velocity of 3 m/s. To obtain the accurate gas velocity, all the cells containing water should be neglected in the calculations and due to the phases being in counterflow this will result in a higher gas velocity than what is specified in the *meanVelocityForce* function.

2.5 Turbulence Model

In some of the more turbulent simulations, Section 3.2 and chapter 5, a turbulence model is utilized. In these simulations the turbulence is modelled using the k-ω-*SST*, *Shear Stress Transport* model [F. Menter, 2003]. It is considered as a robust models which blends the k-ω model in the near wall region and the k-ϵ model in the far field. This is done by multiplying with a blending function and adding both models together. Close to the walls the k-ω model is activated and the blending function have the value one. Far away from the surface the blending fuction takes the value zero which activates the k-ϵ model. The specific boundary conditions used for the turbulence fields k and ω can be found in Appendix B under the respective simulations.[Ansys, 2009]

3 | Solver Validation

In the following chapter a series of transient simulations using periodic boundary conditions are presented and the results are compared to analytical solutions and steady state simulations. This is done to validate the model for a number of different parameters and configurations. The chapter includes validation of the measured specific pressure loss, terminal velocities of water droplets and water volume conservation within the system.

3.1 Specific Pressure Loss

An important parameter for the model to predict accurately is the specific pressure loss. When using periodic boundary conditions the pressure is simply copied between the inlet and outlet patch in every time step. This mean that the pressure difference between inlet and outlet will show in the solution as zero and therefore an alternative method for measuring the pressure loss is required. This is obtained by using the previously mentioned *meanVelocityForce* to control the velocity when using periodic boundary conditions. In this section the specific pressure loss in a duct with a diameter of 50 mm is measured using three different methods in order to validate the model.

The first is the transient case on a small domain using periodic boundary conditions. Three transient simulations have been performed for 1, 3 and 6m/s all with a total simulation time of five seconds. The domain is a small section of a duct with periodic boundary conditions between inlet and outlet and wall with no slip conditions on the sides, as shown in Figure 3.1a. A more detailed description of the computational setup can be found in Appendix B.1. The simulations are conducted using **interCyclicFoam**. The domain is filled with air only and as a result of that there is no difference between **interCyclicFoam** and **interIsoCyclicFoam** in this case as the only difference is in the calculation of the interphase.

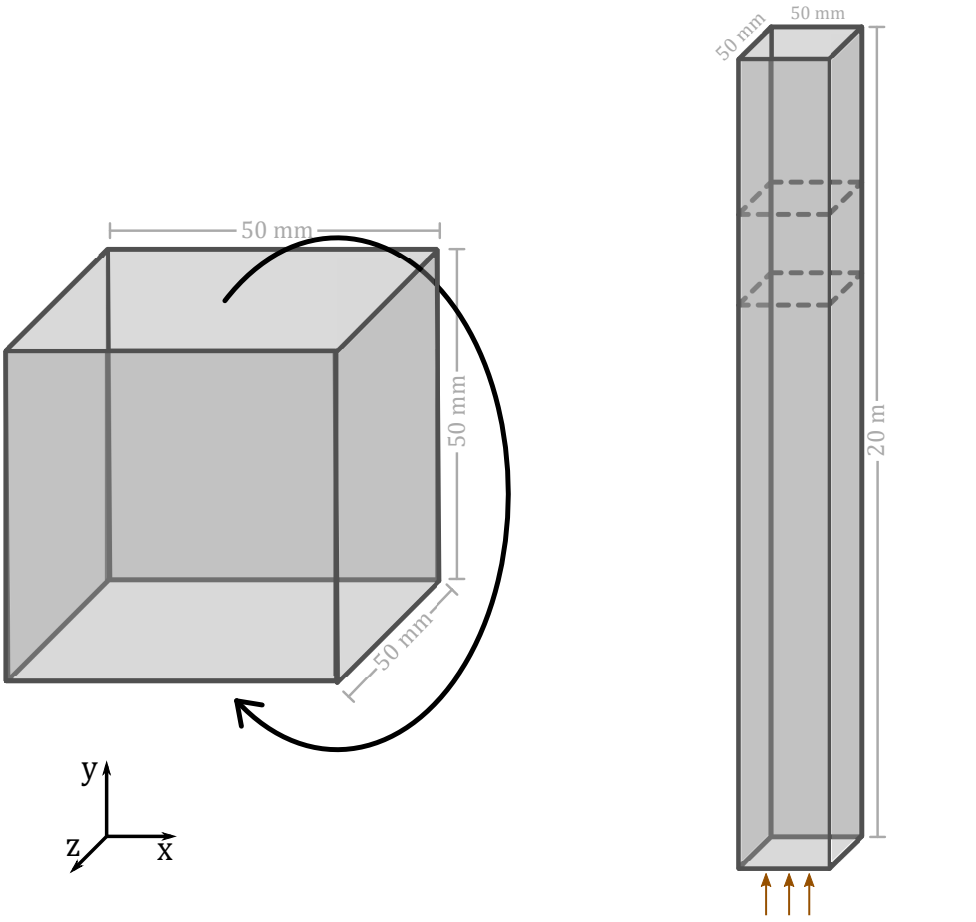

(a) Transient simulation domain. **(b)** Steady state simulation domain.

Figure 3.1: Sketches of the domains used to verify the specific pressure loss. Figure (a) is a small section using periodic boundary conditions between inlet and outlet. Figure (b) is a long duct with a uniform velocity profile at the inlet.

The *meanVelocityForce* is used to define the desired velocity within the domain as, $\bar{U} = (0\,1\,0)$, $\bar{U} = (0\,3\,0)$ and $\bar{U} = (0\,6\,0)$ for the three different velocities. This function adds a source term to the momentum equation and that source term is equal to the specific pressure loss within the system. As the units in the momentum equation is already [Pa/m] the value of the source term can be used directly to describe the pressure loss within the system. The case is a vertical duct and thereby the pressure loss depends on the friction on the walls, which increases with increasing gas velocity, and a constant hydrostatic pressure loss contribution as the air is moving directly against the gravity. The specific pressure loss as a function of time is shown in Figure 3.2. As shown in the graph the specific pressure loss, and thereby also the momentum source term, is highest at the beginning and then slowly decreases towards a constant value. This is because at $t = 0$ the velocity of the air within the system is zero and a higher force has to be added to accelerate the fluid. During the

simulation the specific pressure loss goes towards a constant value. At this point the desired velocity have been reaches and boundary layers have been build on the walls.

When validating the results it is important that the simulation time is sufficiently long to represent fully developed flow. To check when the flow can be considered fully developed Equation 3.1 [Cengel Y, 2012] is used to predict the entry length in a pipe for turbulent flows.

$$\frac{L_\mathrm{h}}{D} = 1.359\,\mathrm{Re}^{1/4} \tag{3.1}$$

Here L_h is the entry length and D is the hydraulic diameter. In the simulation with a gas velocity of 1m/s the entry length is 0.52 m according to Equation 3.1 and the gas moves 5 meters during the simulation. This means that at $t = 5$s the gas have passed ≈ 10 times higher that the predicted entry length according to Equation 3.1. For both 3 and 6m/s the difference between the predicted entry length and the flow travel distance is even larger and the flow is therefore considered to be fully developed.

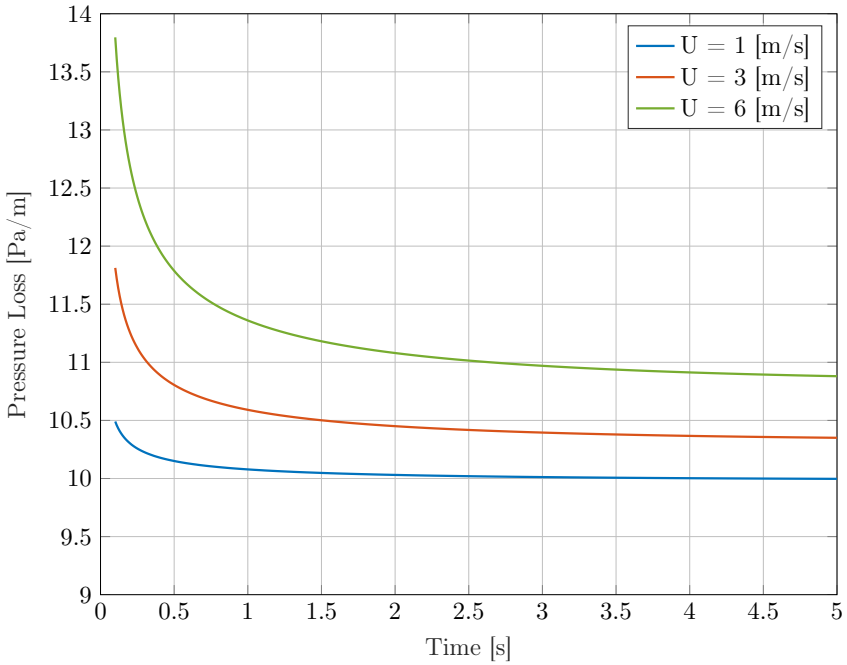

Figure 3.2: Specific pressure loss for different gas velocities as a function of time. The simulations are conducted on a small section of a duct using periodic boundary conditions.

To validate the results of the transient simulations using **interCyclicFoam** shown in Figure 3.2 it is compared to a steady state solution of a long duct. These simulations are conducted using the solver **simpleFoam** within the OpenFOAM enviorment which is a steady state solver for incompressible flow. The domain is a long duct as shown in Figure 3.1b. The inlet boundary is a uniformly distributed velocity profile

with $U_y = 1$, 3 and 6m/s for the three simulations. The specific pressure loss is measured at the end of the duct where a steady flow have been reached. The obtained specific pressure loss from the steady state duct simulations are shown in Figure 3.3 as the dashed lines where the results from both transient **interCyclicFoam** simulation and the steady state simulation using **simpleFoam** are compared.

Furthermore an analytical solution of the specific pressure loss in a duct have been performed using Equation 3.2 and 3.3 [Cengel Y, 2012]. The pressure loss in a vertical duct is a summation of the pressure loss due the wall shear stress and the hydrostatic pressure loss. The friction loss caused by the wall shear stress scales with the gas velocity squared wheres as the hydrostatic pressure loss is a constant value.

$$\Delta P = \underbrace{f \frac{L}{D} \frac{\rho U_{\text{avg}}^2}{2}}_{\text{shear stress}} + \underbrace{\rho g L}_{\text{hydrostatic}} \tag{3.2}$$

$$\frac{1}{\sqrt{f}} = -1.8 \log \left(\left(\frac{\epsilon/D}{3.7} \right)^{1.11} + \frac{6.9}{\text{Re}} \right) \tag{3.3}$$

Here f is the friction factor calculated using the Haaland approximation, L is the length which is one meter to get the specific pressure loss. For the friction factor the surface roughness ϵ is set to zero as no surface roughness is specified in the simulations. The results is shown in Figure 3.3 and compared to the results from both the transient- and steady state simulation.

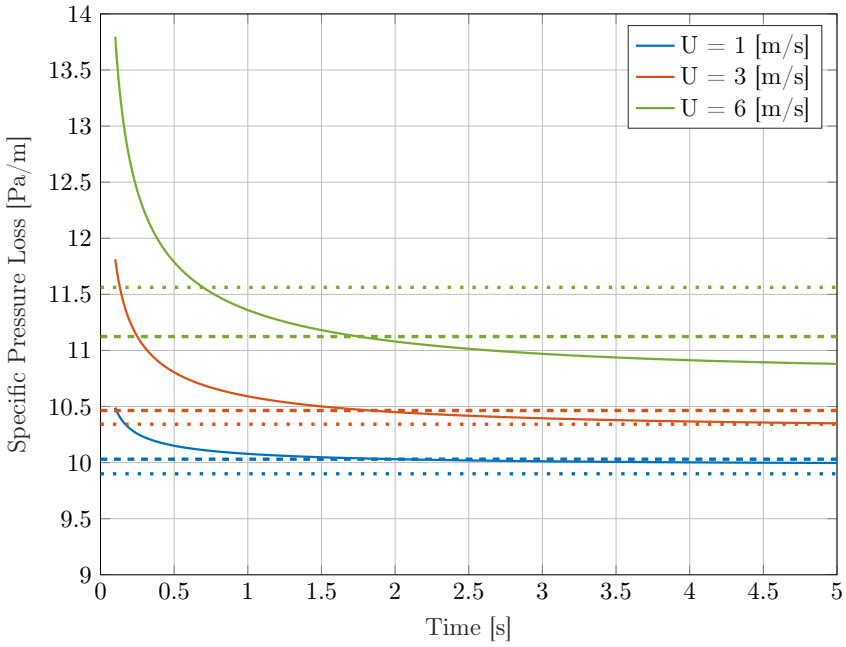

Figure 3.3: Specific pressure loss for different gas velocities as a function of time. The Colored lines are transient simulations on a small domain using periodic boundary conditions, the dashed lines are from steady state simulations in a long duct and the dotted lines are analytical calculations of specific pressure loss for fully developed flows.

From the figure is it shown that the results from the transient simulations are very close to both the steady state solution and the analytical solution for the velocities 1m/s and 3m/s. For the transient simulation at 6m/s the results vary 6.25% compared to the analytical data however the difference between the transient and the steady state results are only 1.4%. The typical velocities encountered in a marine scrubber is around 3m/s and the measurement of the pressure loss using the momentum source term in the transient simulation using **interCyclicFoam** are deemed sufficiently accurate. In cases like this were only a single fluid phase is present in the simulation the two solvers **interCyclicFoam** and **interIsoFoam** are identical as the only difference is in the way the interphase is treated and therefore the validation applies to both models.

3.2 Water Droplet Falling

This section presents a series of transient two-phase simulations using both **interCyclicFoam** and **interIsoCyclicFoam** with periodic boundary conditions in all three dimension. The initial condition is a water droplet surrounded by air exposed to gravitational forces at time zero, this is shown on the left hand side of Figure 3.4. To validate the model the obtained terminal velocity of the droplet is compared to analytical solutions. The definition of terminal velocity is when the summation of

the forces action of the droplet is zero, Equation 3.4. All the forces considered in this setup are illustrated in Figure 3.4 and Equation 3.5 to 3.9.

$$F_{\text{sum}} = F_{\text{b}} - F_{\text{g}} + F_{\text{D}} + F_{\text{s}} = 0 \tag{3.4}$$

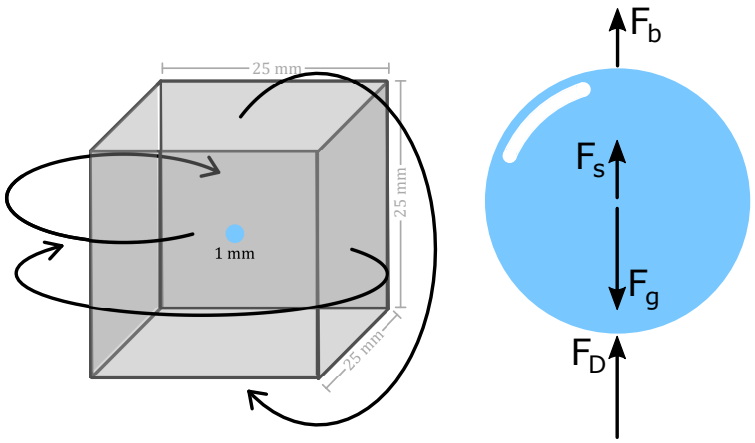

Figure 3.4: Sketch of the computational domain and the the forces acting on the water droplet.

Buoyancy force: Here V is the volume of the droplet. The buoyancy force is constant throughout the simulation assuming the volume of the droplet is constant.

$$F_{\text{b}} = \rho_{\text{air}}\, g\, V \tag{3.5}$$

Gravitational force: Here m is the mass of the water droplet and g is the gravitational acceleration. The gravitational force is also constant throughout the simulation.

$$F_{\text{g}} = m\, g \tag{3.6}$$

Drag force: Here A is the cross sectional area of the droplet sphere ($r^2\,\pi$), u is the velocity of the droplet and C_D is the drag coefficient. For a sphere the drag coefficient is approximated using Equation 3.8 [C. Béguin, 2017]. This is valid for low Reynolds numbers, high viscosity ratios and assumes the droplet to maintain the spherical shape.

$$F_{\text{D}} = \frac{1}{2}\, C_D\, \rho_{\text{air}}\, u^2\, A \tag{3.7}$$

$$C_D = \frac{24}{\text{Re}} \left[1 + 0.15\, \text{Re}^{0.687} + \frac{0.0175}{1 + \frac{42500}{\text{Re}^{1.16}}} \right] \tag{3.8}$$

Source term: This force is introduced due to the periodic boundary conditions. If no actions were taken the movement of the water droplet will accelerate the air surrounding it and the droplet will keep accelerating indefinitely. To make sure that the droplet does reach a constant velocity the *meanVelocityForce* is set to $\bar{U} = (0\,0\,0)$

to ensure that the average velocity in the domain remains zero. This adds a small source term to the momentum equation for every cell in the domain and this can be seen as a force acting on the water droplet in the opposite direction of its movement. This is calculated as the pressure gradient (the momentum source term) times the volume of the droplet. The magnitude of both the source term force and buoyancy force are insignificant compared to the dominant forces drag and gravity.

$$F_{\mathrm{s}} = dp\, V \tag{3.9}$$

Common for all the analytical expression for the forces acting on the droplet is that they all assume mass continuity of the water droplet and in the case of drag force also the sphere shape has to be maintained through time for the correlation of the drag coefficient to be valid. This is only the case for small droplets where the capillary forces are dominant compared to the gravitational forces, represented by a small Bond number, Equation 3.10.

$$\mathrm{Bo} = \frac{4\,\Delta\rho\, g\, r^2}{\sigma} \tag{3.10}$$

According to C. Béguin [2017] water droplets maintain their spherical shape at a Reynolds Number below 300. This corresponds to a droplet with a diameter of 1mm and Bo = 1.5. In the simulation setup a sphere with a radius of 1mm is initialized with a water volumetric fraction of 1 in the center of the domain as shown in Figure 3.4. However due to the selection of cells the resulting water droplet has has a diameter of 1.2 mm, Bo = 2.16 and the Reynolds number at terminal velocity is 439. This is slightly above the criteria specified by C. Béguin [2017] for when a droplet can be considered completely spherical.

The force balance acting on the droplet is used to describe its expected movement including acceleration, velocity and distance traveled, Equation 3.11 to 3.13. The equations are solved numerically with $\Delta t = 0.001$s to obtain the movement as a function of time. The acceleration of the water droplet is a function of the summation of the forces acting on the droplet and its mass, Equation 3.11. This acceleration is used to describe the velocity of the droplet for the next iteration, Equation 3.12 and finally the distance traveled is calculated using both the acceleration and velocity of the droplet in Equation 3.13.

$$a_i = \frac{F_{\mathrm{sum,i}}}{m} \tag{3.11}$$

$$U_{i+1} = U_i + a_i\, \Delta t \tag{3.12}$$

$$y_{i+1} = y_i + U_i\, \Delta t + \frac{1}{2}\, a_i\, \Delta t^2 \tag{3.13}$$

Here a is the acceleration of the droplet, m is the mass, U is the velocity, y is the distance in the y-direction and Δt is the time step per iteration. The expected

results using the analytical solution for distance, velocity and acceleration are shown in Figure 3.5 as a function of time.

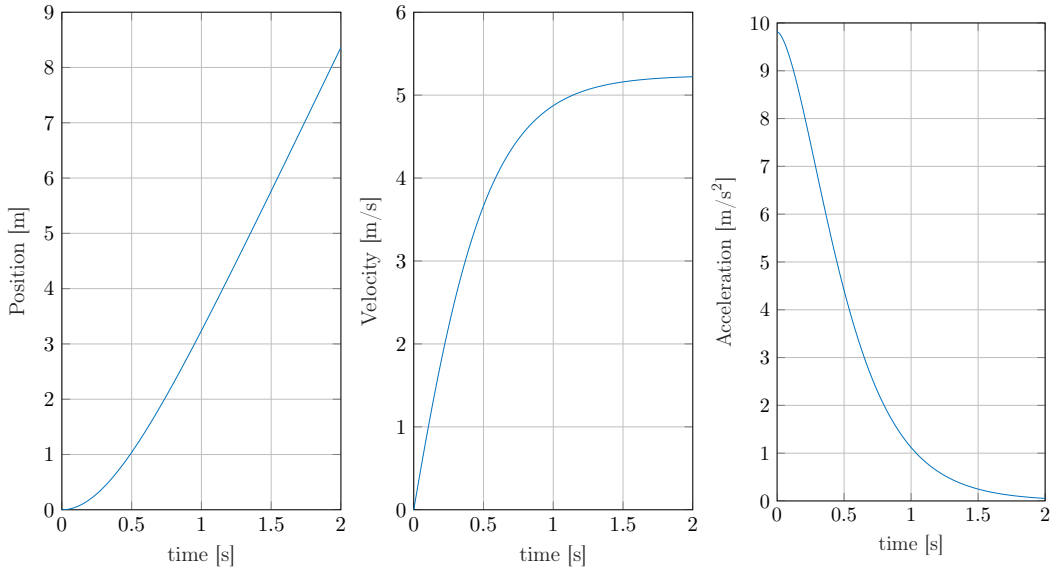

Figure 3.5: Distance traveled, velocity and acceleration of the water droplet as a function of time using the analytical solution.

For the transient CFD simulations they are all conducted on an initially coarse mesh with outer domain as show in Figure 3.4. The cells are all 0.5x0.5x0.5 mm resulting in a total of 125 000 cells. During the simulation the mesh is refined in the interphase between water and gas to improve the sharpness of the interphase. This refinement are done for all the cells where $0.001 < \alpha_{\text{water}} < 0.999$ which is considered interphase cells. A more detailed descriptions of the computational setup for these simulations can be found in Appendix B.2. In Figure 3.6 the velocity of the water droplet is plotted as function of time for three different computational setups and compared to the analytical solution. The black line is the analytical solution and is the same velocity plot as shown previously in Figure 3.5. The first transient simulation is represented by the blue curve and uses the **interCyclicFoam** solver. In this simulation the dynamic mesh refinement are used to refine the cells in the interphase between water and gas. The refinement level is set to 2 which means that the solver refines the cells in the interphase by halving them in all directions two times. With a refinement level of 2, the original cells with the dimensions 0.5 x 0.5 x 0.5mm gets refined to a larger number of cells with the size 0.125 x 0.125 x 0.125mm. By doing this refinement the number of cells in the interphase gets increased by a factor of 64 which drastically improves the sharpness of the interphase. The second simulation represented by the red curve in Figure 3.6 also uses the **interCyclicFoam** solver, but the interphase is refined even more. The refinement level is increased from 2 to 3 resulting in cells in

the interphase with the size 0.0625 x 0.0625 x 0.0625mm. For this simulation the number of cells to describe the interphase is increased by a factor of 512. The final simulation represented by the green curve uses the **interIsoCyclicFoam** solver and a refinement level of 2. The only difference between the two solvers **interCyclicFoam** and **interIsoCyclicFoam** is in the calculation of the interphase between the water and gas. According to Roenby J [2016] the **interIsoCyclicFoam** solver should achieve as sharper interphase than the **interCyclicFoam** on the same mesh.

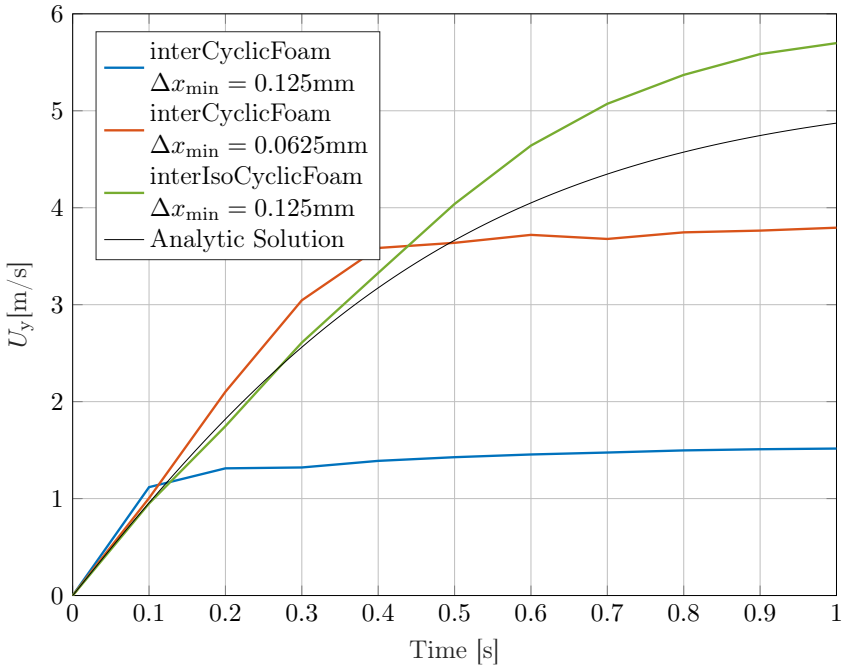

Figure 3.6: A comparison of the droplet velocity as a function of time for the three simulations and the analytical solution.

As shown in Figure 3.6 there is a significant difference in the velocity of the water droplet depending of how refined the interphase is and between the two solvers. To investigate what causes these differences between the computational setups, slices of the simulation results after one second are shown in Figure 3.7. It shows a clear difference in the sharpness of the interphase for different refinement levels, Figure 3.7a and 3.7b. The resulting velocity of the droplet is 1.516 m/s and 3.79 m/s respectively for the to simulations using **interCyclicFoam** compared to the analytical solution of 4.87 m/s. By comparing the pictures of the droplet after one second is it clear that the droplet is more well defined with a more clear interphase in the simulations with the higher refinement level, but also the interior cells is significantly different. In Figure 3.7a the interior cells does not reach a water volumetric fraction of 1. This means that the water droplet in the simulation only consist of $\approx 80\%$ water and the rest being air. As the physical properties for each cells is calculated as a weighted

average of the α_{water} value of the cell, the density will decrease for the cells that does not reach $\alpha_{\text{water}} = 1$. The lower density will result in a lower gravitational force acting on the individual cells and is a big factor why the velocity of the droplet is significantly lower that the analytical solution, shown by comparing the blue curve in Figure 3.6 to the analytical solution represented by the black curve. However when the mesh in the interphase is further refined, the red curve in Figure 3.6 and 3.7b, all the interior cells have $\alpha_{\text{water}} = 1$ which they should as it means that the droplet is all water. This also yields a significant increase in the obtained droplet velocity which after 1 second is 22% lower than the analytical solution.
The results using the **interIsoCyclicFoam** solver shown in Figure 3.7c does not have any issues with the interior cells having $\alpha_{\text{water}} < 1$ and the droplet is well defined compared to Figure 3.7a. This results in a droplet velocity after one second for the **interIsoCyclicFoam** case at 5.7 m/s which is 17% higher than the expected value of 4.87 m/s.

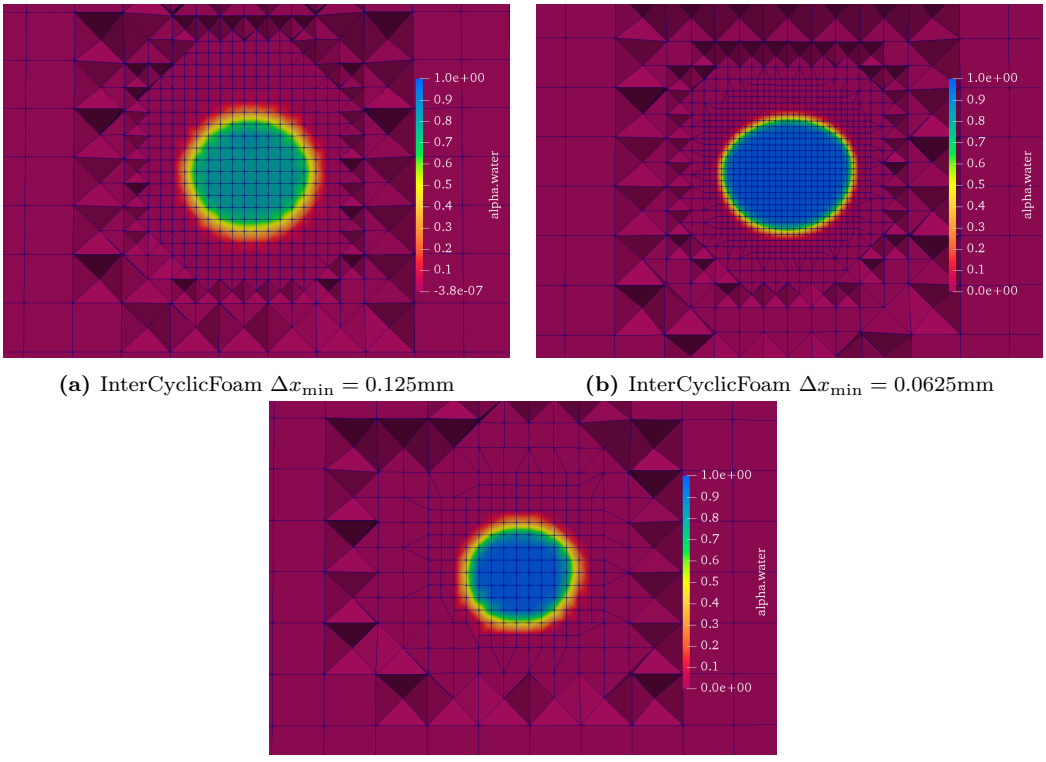

(a) InterCyclicFoam $\Delta x_{\text{min}} = 0.125\text{mm}$

(b) InterCyclicFoam $\Delta x_{\text{min}} = 0.0625\text{mm}$

(c) InterIsoCyclicFoam $\Delta x_{\text{min}} = 0.125\text{mm}$

Figure 3.7: The α_{water} cell values for the three simulations after one second of simulation time.

An important performance criteria of the solver is to conserve the water volume within the system during the simulation. According to the analytical solution the water droplet should move 3.2 m over the one second of simulation time. This corresponds to 128 times through the small domain and it is important that the water volume is

conserved each time it passes through the periodic boundary. In Figure 3.8 the water volume, represented by the diameter of the water droplet, is plotted as a function of time for each simulation.

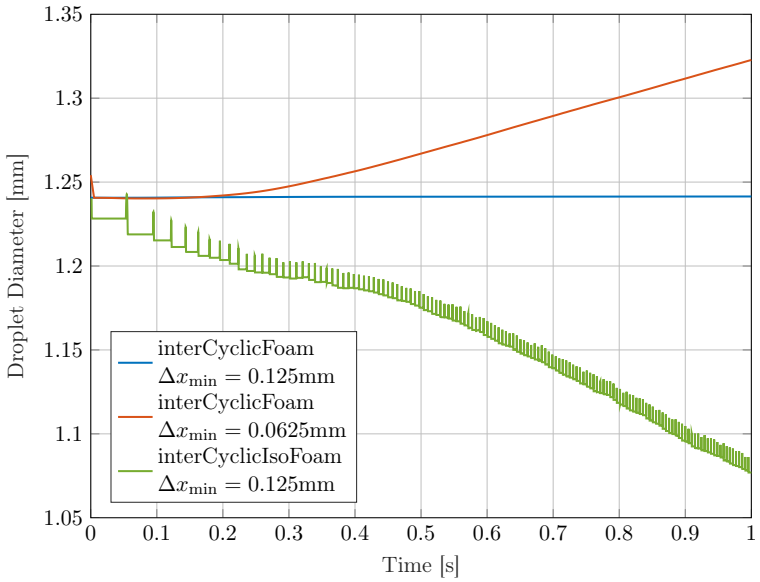

Figure 3.8: Water volume as a function of time for the three simulations represented by the droplet diameter assuming a perfect spherical shape.

As shown in the figure the water volume is accurately conserved in the interCyclicFoam simulation with $\Delta x_{\min} = 0.125$mm. When the cells is refined to $\Delta x_{\min} = 0.0625$mm however, the total water volume starts gradually increasing over time. This may be caused by rounding error in the refinement process that is taking place during the simulation. The higher volume of the droplet should result in a higher terminal velocity, but not to the extent shown as the difference between the two **interCyclicFoam** simulations in Figure 3.6.
For the **interIsoCyclicFoam** solver the water volume is decreasing throughout the entire simulation. The many spikes in the graphs corresponds to the 128 times the droplet passes through the periodic boundary conditions. This indicates that the problem occurs in the process of copying the interphase over the periodic boundaries when using the isoAdvector scheme in the **interIsoCyclicFoam** solver.

Based on the simulations done in this section it can be concluded that when using the **interCyclicFoam** solver a very fine mesh is required to obtain an accurate representation of the water droplet and its movement over time. It is also important to note that if the mesh is refined to much locally, which was the case in Figure 3.7b and shown as the red curve in Figure 3.8, numerical errors can occur that breaks the continity of the system in terms of water volume conservation. In order to avoid these

issues the difference in cells sizes in the domain can not become to large.
For the **interIsoCyclicFoam** solver the representation of the droplet and its movement is much closer to the expected values than the **interCyclicFoam** solver for the same mesh refinement. However the water volume is not properly conserved when the droplet passes through the periodic boundary conditions. This means that for cases where the droplet only needs to go through the periodic boundary conditions a couple of times the **interIsoCyclicFoam** is superior as it does not require as fine a mesh to obtain accurate results. On the other hand if the water have to pass through the periodic boundary conditions many times to achieve a steady solution the **interIsoCyclicFoam** solver is not valid due to poor water conservation and the **interCyclicFoam** solver has to be used instead.

4 | Droplet-solid interactions

In the following chapter the waters interaction with solid surfaces is investigated. In the design of a scrubber the interfacial area between gas and water is of great interest as it enhances the SO_x removal. This is the reason the absorption column is filled with a number of filling elements. Under operation they are covered by a thin water film layer which drastically increase the interfacial surface area between the water and gas. The thickness of the water film is controlled by the surface wettability. This is not a property of the liquid only as it also depends on the roughness and chemical composition of the solid. The chapter includes descriptions and simulations of the effect of different contact angles on the interphase area of a water droplet on a solid surface, the behaviour of water droplets colliding with solid surfaces at varying velocities and finally the dynamics of water droplets moving along an inclined solid surface.

4.1 Water-Solid Contact Angle

The wettability can be described by the contact angle of a water droplet of a solid surface. Figure 4.1 shows a sketch of a water droplet in 2D on a solid surface with the contact angle θ.

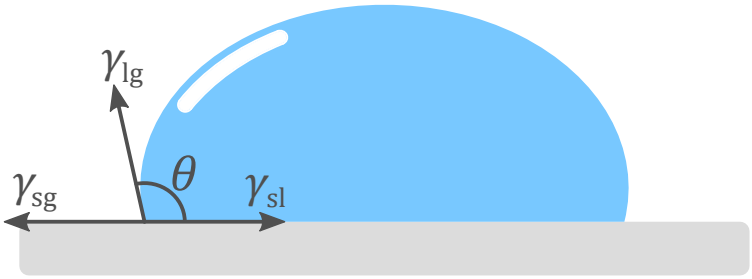

Figure 4.1: A sketch of a droplet at rest on a solid surface.

For a droplet in equilibrium the contact angle is measured on the air-water-solid line, also called the three-phase contact line. On this line the droplet is force balanced in the tangential direction. The contact angle can be estimated using Young's Equation shown in Equation 4.1. [Guoli Li, 2020]

$$\cos\theta = \frac{\gamma_{sg} - \gamma_{sl}}{\gamma_{lg}} \tag{4.1}$$

Here θ is the contact angle and γ_{sg}, γ_{sl}, γ_{lg} represents the solid-gas, solid-liquid and liquid-gas interfacial tensions respectively. The contact angle given by Young's equation is a thermodynamic property of a three-phase system which represents the lowest state of energy for the system. A low contact angle corresponds to a high wettability which results in a thin film on a solid surface. On the other hand a high contact angle

corresponds to a low wettability and a thicker film. Normally $\theta < 90°$ is considered hydrophilic and $\theta > 90°$ is hydrophobic.

Within OpenFOAM the contact angle on solid surfaces is specified by utilizing the *constantAlphaContactAngle* boundary condition for the α_{water} field. A series of simulations have been conducted to see the influence the contact angle has on a water droplet at equilibrium on a solid surface. A water droplet with a diameter of 2 mm is exposed to gravity at $t = 0$ and are hitting the solid surface at a low velocity. A more detailed describetion of the computational setup for these simulations can be found in Appendix B.3. The initial- and equilibrium state for three different contact angles are shown in Figure 4.2 using isosurfaces and a z-normal slice in Figure 4.3.

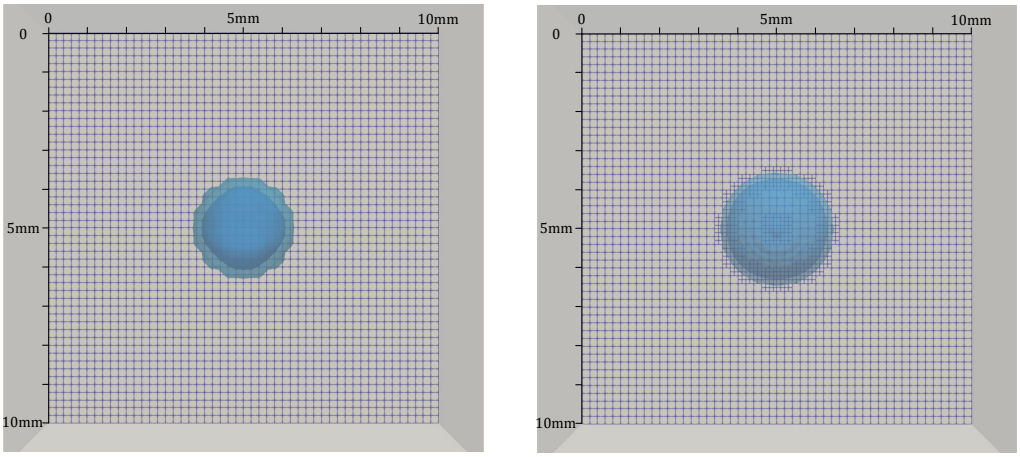

(a) Initial condition at $t = 0$

(b) $\theta = 90°$

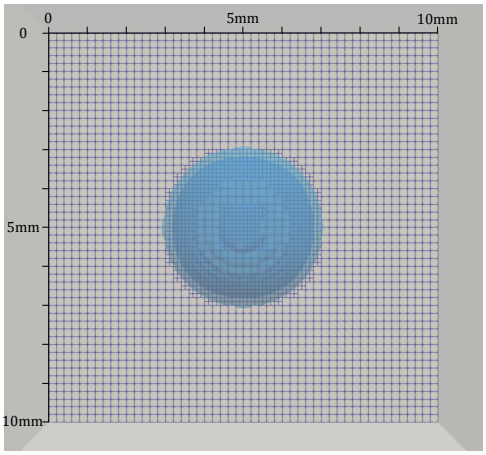

(c) $\theta = 45°$

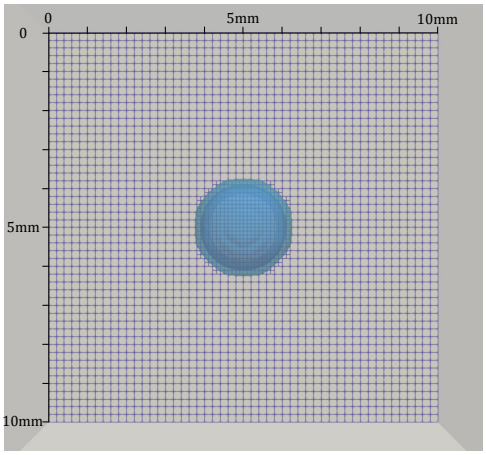

(d) $\theta = 135°$

Figure 4.2: Water droplets with $D = 2$mm at $t = 0$ is exposed to gravity figure (a). Figure (b), (c) and (d) are the equilibrium state for three different contact angles. The droplet is represented by isosurfaces, the dark blue at $\alpha_{\text{water}} = 0.5$ and the light blue at $\alpha_{\text{water}} = 0.001$

.

It is clear from Figure 4.2 that with a lower contact angle the water droplet will occupy a larger area on the solid surface. This is in agreement with the statement that a low contact angle represents a solid surface with a high wettability and vice versa.

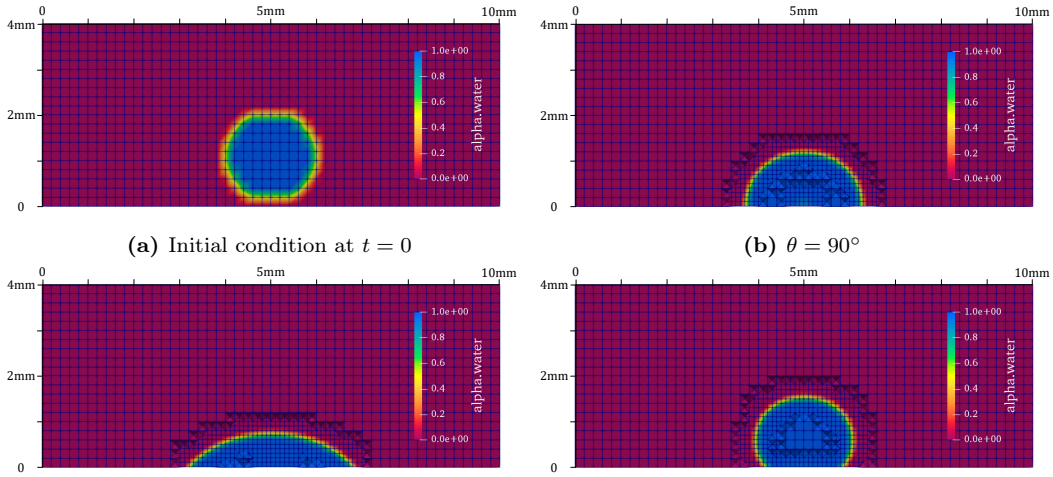

(a) Initial condition at $t = 0$

(b) $\theta = 90°$

(c) $\theta = 45°$

(d) $\theta = 135°$

Figure 4.3: Water droplets with $D = 2$mm at $t = 0$ is exposed to gravity figure (a). Figure (b), (c) and (d) are the equilibrium state for three different contact angles. The droplet is represented by the interpolated α_{water} field values on a z-normal slice through the middle of the domain.

Consider a water droplet at rest on a solid surface as shown in Figure 4.1. If the gravitational force acting on the droplet is not significant compared to the surface tension forces its shape can be considered as a spherical cap. Analytical solutions for the volume and surface area of the droplet under these assumptions is presented by Yukihiro Yonemoto [2020] as shown in Equation 4.2 to 4.4.

$$A_{\text{surface}} = \frac{2\,\pi\,h^2}{1 - \cos(\theta)} \tag{4.2}$$

$$V = \pi\,h\left(\frac{h^2}{6} + \frac{R^2}{2}\right) \tag{4.3}$$

$$h = \frac{R\,(1 - \cos(\theta))}{\sin(\theta)} \tag{4.4}$$

Here A_{surface} is the surface area of the droplet, V is its volume and θ is the contact angle. The parameters h and R are the droplet height and contact area radius respectively as shown in Figure 4.4.

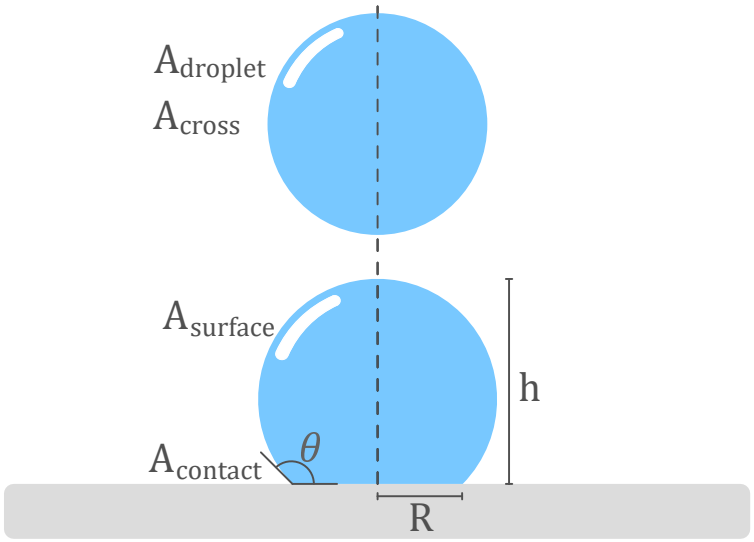

Figure 4.4: Sketch of a water droplet hitting a solid surface with contact angle 130°.

Under the assumptions that the droplet can be treated as a spherical cap the dimensions of the droplet at rest on a solid surface only depends on the initial volume which is conserved and the contact angle. In Equation 4.5 to 4.7 the dimensionless property ϕ_1 is presented as the fraction between the surface area of the droplet on the surface and contact area between the water and the surface. It is shown that ϕ_1 only depends on the contact angle and the results is valid for all droplet sizes under the assumption that the gravitational forces can be neglected.

$$\phi_1 = \frac{A_{\text{surface}}}{A_{\text{contact}}} \tag{4.5}$$

$$= \frac{\left(\frac{2\,\pi\,h^2}{1-\cos(\theta)}\right)}{\pi\,R^2} \tag{4.6}$$

$$= \frac{2\,(1-\cos(\theta))}{\sin(\theta)^2} \tag{4.7}$$

The results of ϕ_1 is shown in Figure 4.5 as a function of contact angle. Furthermore the figure includes the ratio between droplet surface area at rest and the initial droplet area ϕ_2 and the ratio between the contact area and initial cross sectional area of the droplet ϕ_3. They all only depends on the contact angle assuming mass conservation and neglecting the gravitational forces.

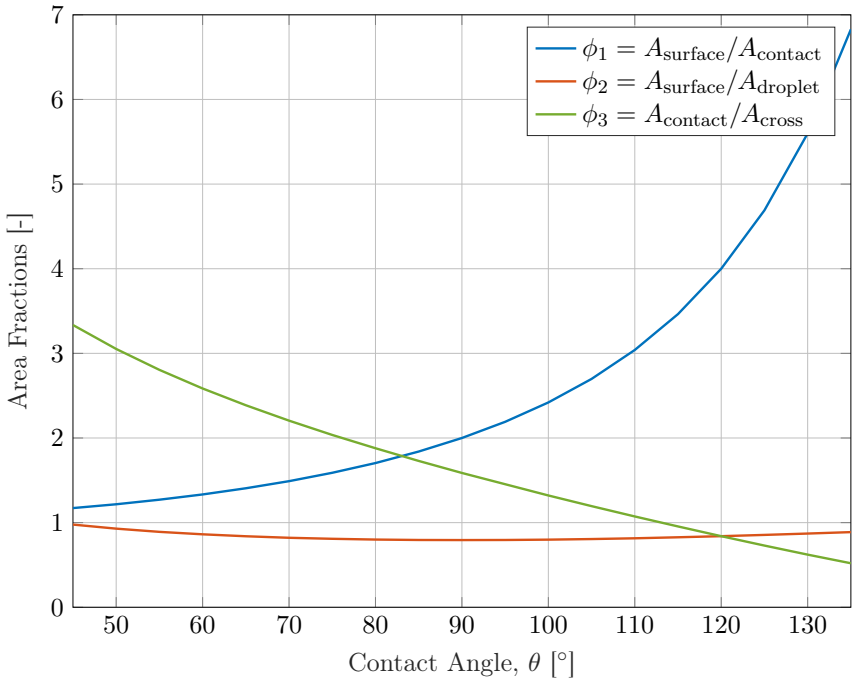

Figure 4.5: Area fractions as a function of contact angle when neglecting gravitational forces and assuming mass conservation.

As shown in the figure ϕ_2 is almost constant at one with a contact angle in the range 45°to 135°. This means that there is only a small difference between the surface area of a spherical water droplet and when its at rest on a solid surface. The lowest point for ϕ_2 is 0.79 at 90°which is the lowest surface area a droplet on a solid surface can have. The variable ϕ_1 on the other hand changes significantly with increasing contact angle. This shows that with a higher contact angle the surface area of the droplets gets higher compared to the area it occupies on the solid surface. The last variable ϕ_3, which is the ratio between contact area and the initial cross sectional area of the droplet, decreases with a higher contact angle. At 45° the area the droplet occupies on the solid surface is 3.3 times higher than the initial cross sectional area. This reduces to 1.6 at 90° and ends at 0.5 at 135°. At this point the water-solid contact area is only half of the the initial cross sectional area of the droplet.

As mentioned before Equation 4.2 to 4.4 and Figure 4.5 are only valid when the gravitational forces acting on the droplet can be neglected. The Bond number $\text{Bo} = 4\,\Delta\rho\,g\,r^2/\sigma$ is a dimensionless number of the fraction between gravitational forces and surface tension forces. As presented previously in Section 3.2 for the shape of the water droplet to be considered spherical the surface tension forces have to be dominant over the gravitational forces represented by a small Bond number. In Figure 4.6 four simulation results are presented where the Bond number is varied by changing the initial droplet diameter in the range 1 mm to 4 mm. The droplets at force equilibrium

is shown in z-normal slices through the middle of the domain and compared to the analytical solution of the spherical shape when neglecting gravitational forces acting on the droplets.

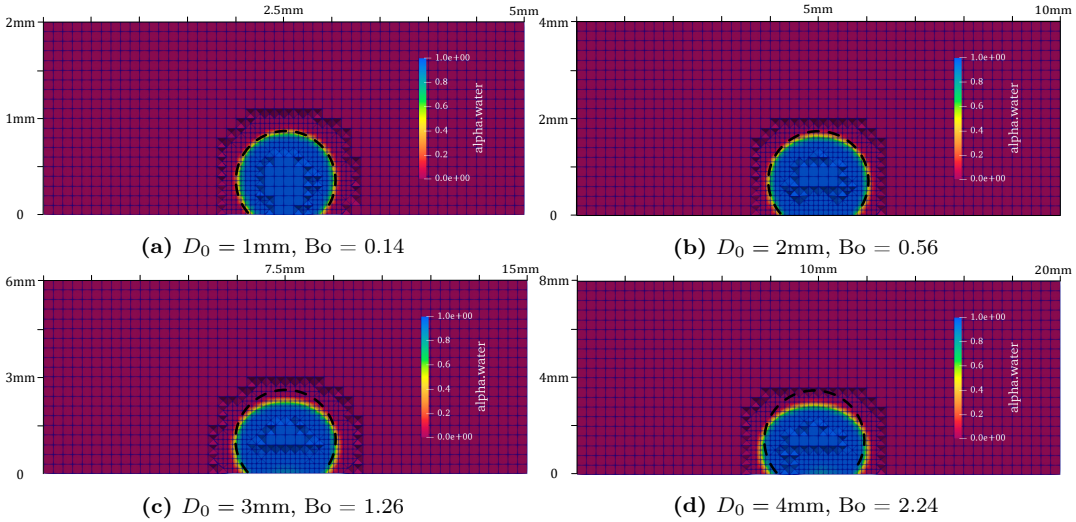

(a) $D_0 = 1\text{mm}$, Bo $= 0.14$ **(b)** $D_0 = 2\text{mm}$, Bo $= 0.56$

(c) $D_0 = 3\text{mm}$, Bo $= 1.26$ **(d)** $D_0 = 4\text{mm}$, Bo $= 2.24$

Figure 4.6: Water droplets at force equilibrium for different initial droplet diameters. The contact angle is 130°. The dashed line is the expected spherical shaped neglecting gravitational forces.

As shown in Figure 4.6a and 4.6b the analytical solution of the droplet shape fit very well at the low droplet sizes and Bond numbers. However when the droplet size is increased, Figure 4.6c and 4.6d, larger differences between the analytical solution and the actual droplet shape can be observed. The gravitational forces becomes more dominant and the droplet at force equilibrium becomes more and more flat as a result of that. From the simulations it is clear that the analytical solution of the droplet shaped that neglects the gravitational forces is only valid for small droplets with Bo < 1.

Based on the simulations done in this chapter it can be concluded that a higher wettablility of the solid surface, represented in the simulations by a low contact angle, results in a higher contact area between water and surface. The ration between the surface area of a water droplet at rest on a solid surface and the contact area increases with a higher contact angle, however the ratio between the surface area before and after impact are almost independent of the contact angle. It was also shown that for small droplets where the surface tension forces are dominant over the gravitational forces, represented by Bo < 1, the shape of the water droplet at rest on a solid surface can be considered a perfect spherical cap.

4.2 Spreading Factor

This section investigates the fluid behaviour when a water droplet hits a solid surface at a given velocity. When the droplet hits the surface it creates a radially expanding film flow. The diameter of the film on the surface will increase until the maximum spreading diameter is reached, assuming the droplet does not split up under impact with the solid. If the solid surface is partially or nonwettable the droplet recedes after the maximum spreading diameter is reached. Many studies have been conducted to make correlations to predict the droplet behavior when impacting a solid surface. The term maximum spreading factor $\beta_{\max}$, is used as a dimensionless number to describe the ratio between the maximum spreading diameter and the diameter of the water droplet just before impact. The spreading factor can be estimated based on the impact parameters: contact angle θ, the Reynolds number $\mathrm{Re} = \rho D_0 U_0/\mu$ and Weber number $\mathrm{We} = \rho D_0 U_0^2/\sigma$, with D_0 and U_0 being the impact droplet diameter and velocity respectively.
The simplest correlation for the maximum spreading factor is presented by Roisman [2009] as shown in Table 4.1. It only depends on the Weber number and therefore does not account for the viscosity of the fluid. As a result of that the correlation is only valid for low-viscosity fluids defined by $\mathrm{We}\,\mathrm{Re}^{-4/5} < 1$. Later in the study, Roisman [2009] presents a semiempirical relation also shown in Table 4.1 that includes the dampening effect of the viscous forces by introducing the Reynolds number. Other studies have also included the affect of the fluid viscosity. One of these is Ilkers Bayer [2006] who investigated the impact of wetting characteristics of a solid substrate on the droplets impact behaviour. The results showed that the maximum spreading factor was relatively insensitive to the wetting characteristics on the solid surface which is also in agreement with Roisman [2009]. The equation for the maximum spreading factor is shown in Table 4.1 after correlating with $\mathrm{Re}\,\mathrm{We}^{1/2}$. Finally Jia-Meng Tian [2019] made a correlation based on a number of experiments with four different liquids, R113, deionized water, ethanol and acetone. The study showed that a high impact velocity, low liquid viscosity and low surface tension will produce a large spreading capability.

Table 4.1: Spreading factor approximations

Reference	Correlation for $\beta_{\max}$
Roisman [2009] (simple)	$\beta_{\max} = \mathrm{We}^{1/4}$
Roisman [2009]	$\beta_{\max} = 0.87\,\mathrm{Re}^{1/5} - 0.4\mathrm{Re}^{2/5}\,\mathrm{We}^{-1/2}$
Ilkers Bayer [2006]	$\beta_{\max} = 0.72\left(\mathrm{Re}\,\mathrm{We}^{1/2}\right)^{0.14}$
Jia-Meng Tian [2019]	$\beta_{\max} = 0.09\left(\mathrm{Re}\,\mathrm{We}^{1/2}\right)^{1/3}$

The correlations for $\beta_{\max}$ mentioned in Table 4.1 are plotted as a function of impact velocity in Figure 4.7 for a water droplet with diameter of 2 mm. From the figure it is shown that the spreading factor increases with increasing impact velocity for all

four correlations. The difference between them are highest at low impact velocity whereas the agreement becomes better when the velocity increases for these specific droplet properties.

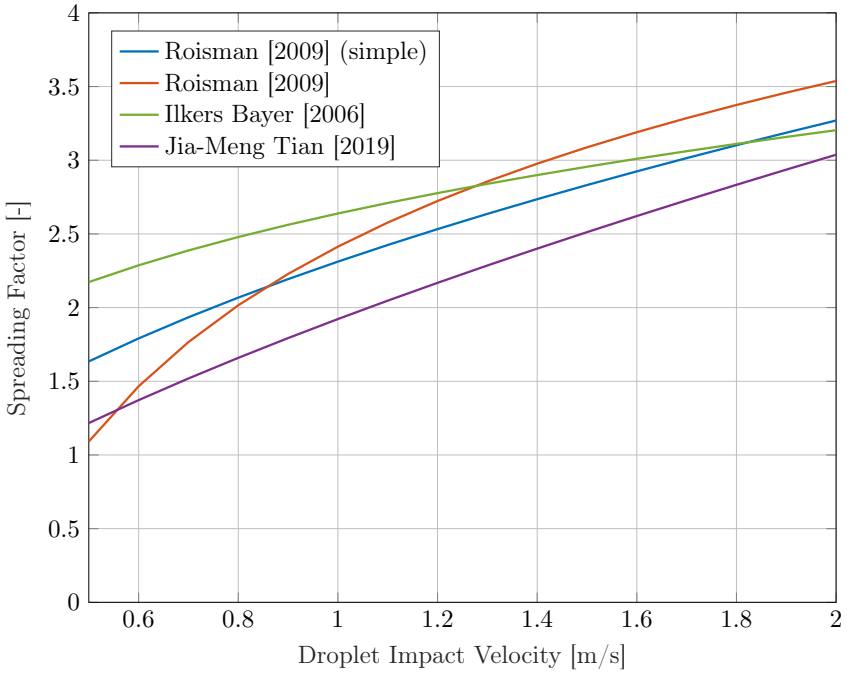

Figure 4.7: Spreading factor as a function of droplet impact velocity for four different correlations.

In this study a series of CFD simulations is used to obtain the maximum spreading factor at varying impact velocity. All the simulations presented here uses the **interCyclicFoam** solver. The initial state at $t = 0$ is a water droplet right above a solid surface with a specified velocity in the downwards direction. The contact angle is specified as constant 130° which is a rough estimate made by Roisman [2009] if the Weber number and Reynolds number are high. In the range 0.5m/s to 2 m/s for the impact velocity the Weber number and Reynolds number are 7 to 114 and 1000 to 4000 respectively when using the properties of water. Similar to the previous simulations the utility *dynamicMeshRefine* is used to further refine the cells in the liquid-gas interphase. A more detailed description of the computational setup can be found in Appendix B.3. The simulation results for the case with impact velocity 1m/s is shown in Figure 4.8 at four different time steps. The maximum diameter on the solid surface is reached at $t = 3$ms and after that point the droplet recedes due to the surface tension forces.

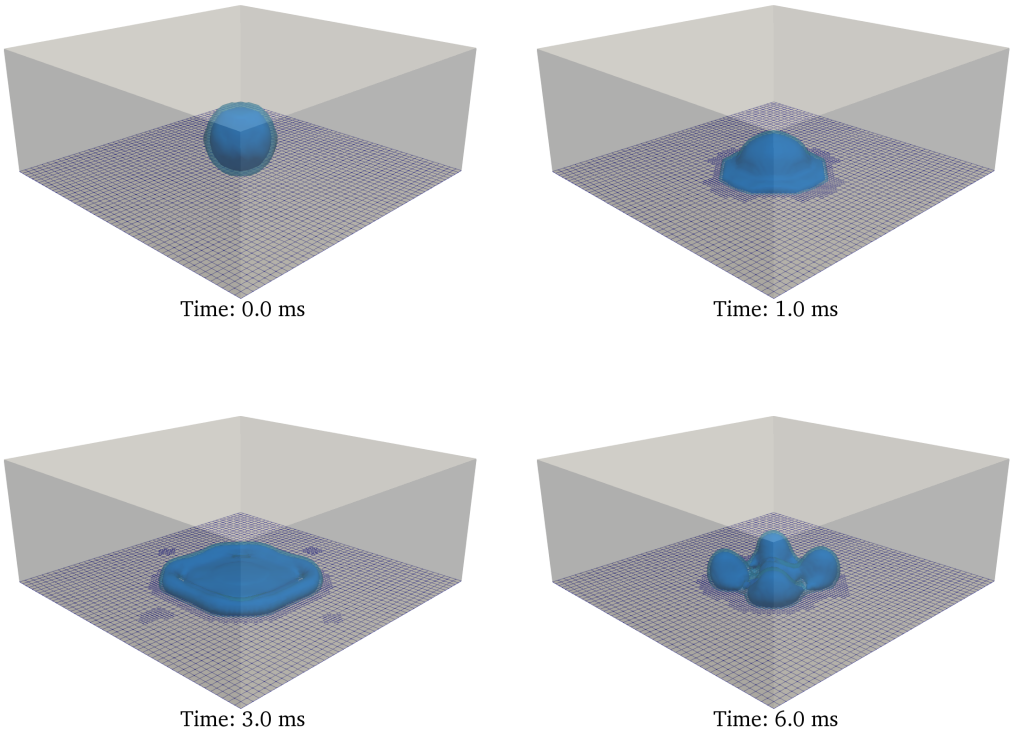

Figure 4.8: A water droplet with a diameter of 2mm hitting a solid surface with $\theta = 130°$. The impact velocity is 1 m/s.

In Figure 4.9 the simulations results is shown at the time where the largest spreading diameter is reached. The simulation results are compared to the four correlations from Table 4.1 for an impact velocity of 0.5m/s and 1m/s shown as the dashed circles in the figure.

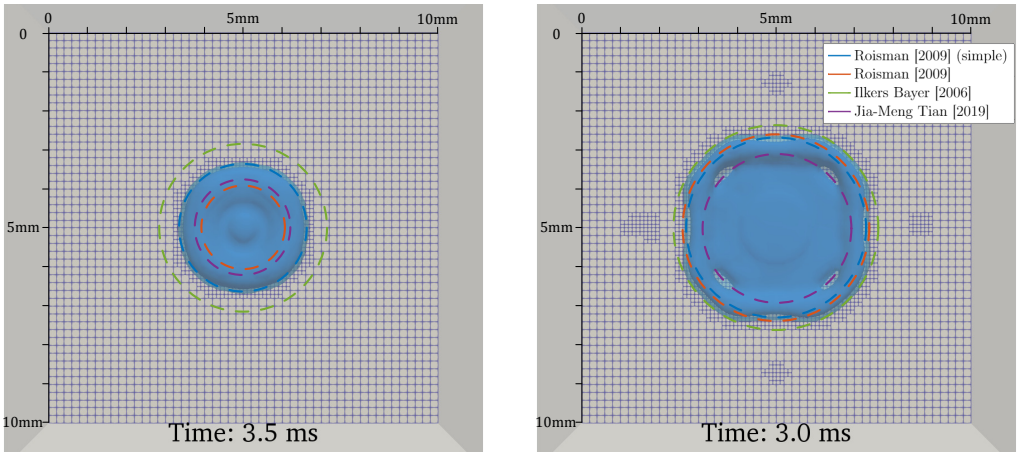

(a) $U_{\text{impact}} = 0.5\text{m/s}$ **(b)** $U_{\text{impact}} = 1\text{m/s}$

Figure 4.9: The water droplet shown from above at the maximum spreading. The dark blue is isosurface at $\alpha_{\text{water}} = 0.5$ and the light blue is at $\alpha_{\text{water}} = 0.1$. The dashed circles are the spreading factor obtained by empirical correlations.

The two correlations presented by Roisman [2009] fits the simulations results well at an impact velocity of 1m/s. However when the impact velocity is lowered to 0.5m/s the second correlation from Roisman [2009], which includes the viscous forces, under predicts the spreading diameter while the simple correlations still fits the simulations results well. The correlation in Ilkers Bayer [2006] predicts the highest spreading diameter for both cases compared to the other correlations. With a impact velocity of 1m/s the the predicted value if only slightly higher than the simulations results whereas with an impact velocity of 0.5m/s the difference between the correlation and simulations results are more significant. For the final empirical correlation presented by Jia-Meng Tian [2019] the model under predicts the spreading radius significantly in both simulations. From the comparison in Figure 4.9 it is clear that the simple correlations in Roisman [2009] is the best fit for the simulation results when considering both impact velocities. All the correlations presented in the section are based on experimental studies and differences in the experimental setup and surface material used can explain some of the differences in the results. In the simulations the contact angle on the solid surface is defined as 130° which was stated in Roisman [2009]. Even though most of the studies states that the spreading radius is relatively insensitive to the wetting characteristics of the solid surface (the contact angle) this can still explain some of the differences between the correlations.
It can be concluded that the simulation results are within the range of the four empirical correlations presented for both cases and the model seems to capture the dynamic behaviour sufficiently accurate. Comparing the two simulations it is clear that there is a significant difference is the spreading diameter based on the impact velocity which was to be expected based on the experimental results from the other studies.

4.3 Dynamic Behaviour

In this section the dynamic behaviour of water droplets movement along an inclined solid surface have been investigated. With the geometry of the filling elements used in the absorption column the water interacts with a variety of inclination angles and it is investigated in this section how this can be translated to the numerical model. A series of simulations with varying droplet size and surface inclination angles have been conducted. The simulation results is validated against experimental data from another study.

For a droplet that vertically hits a horizontal solid surface, the contact angle on the surface is assumed constant for the entire droplet. However on an inclined surface where the droplet is moving alongside it there is a difference in contact angle from the leading to the trialling edge. This is illustrated in Figure 4.10 with a droplet on a surface with the inclination angle α. The highest contact angle is observed at the leading edge of the droplet and is called the advancing contact angle θ_a whereas the lowest is at the trailing edge and is called the receding contact angle θ_r.

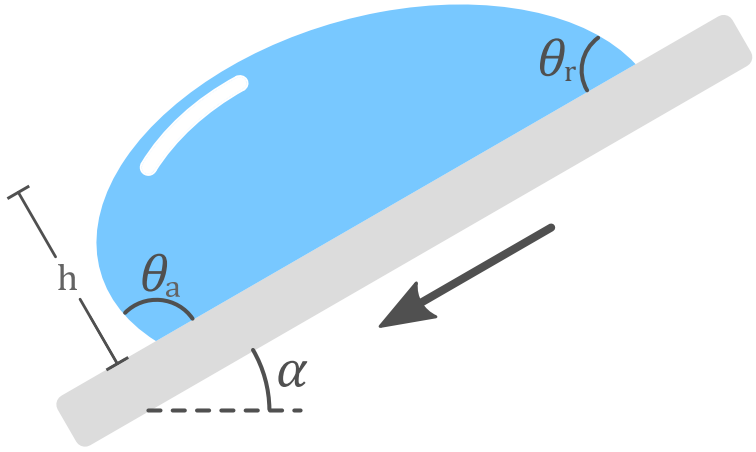

Figure 4.10: A sketch of a droplet on an inclined surface showing the advancing and receding contact angles between the water and the solid.

As with the contact angle on horizontal surfaces θ_a and θ_r depends on the physical properties of the fluid and the surface. However it also depends on the size of the droplet, measured by its volume V_d, and the inclination angle α of the surface. In reference Abdullah Al-Sharafi [2020] the advancing and receding contact angles on a hydrophilic surface are provide for droplets in the range 5µL to 25µL and inclination angles 10° to 90°. In this study four simulations have been carried out for droplet size 15µL to 25µL and inclination angles 20° to 60°. The corresponding advancing and receding contact angles according to Abdullah Al-Sharafi [2020] are listed in Table 4.2.

Table 4.2: Advancing and receding contact angles water droplets on inclined hydrophilic surface for various droplet size and inclination angles.

	$V_\mathrm{d} = 15\mu\mathrm{L}$		$V_\mathrm{d} = 25\mu\mathrm{L}$	
	θ_A	θ_R	θ_A	θ_R
$\alpha = 20°$	84.35°	75.7°	90.81°	73.7°
$\alpha = 60°$	93.62°	65.18°	98.5°	60°

The simulations uses **interCyclicFoam** as the solver on a small domain with the dimensions 10mm x 4mm x 8mm. The bottom of the domain is a no-slip wall boundary with the *dynamicAlphaContactAngle* condition for the α_water field based on the data in Table 4.2. The inclination angle of the surface is controlled by varying the direction of the gravitational force. This allows a parametric study of the inclination angle without changing the domain itself. The simulation results for the four simulations are shown in Figure 4.11 for both a 3D view with the droplet represented by interpolated isosurfaces and a slice though the middle of the domain showing the interpolated α_water field values. The droplet is moving from the right hand side of the domain towards the left. The left and right boundary of the domain are periodic boundaries that allows the simulation of a long surface while still using a small computational domain. More details about the computational setup can be found in Appendix B.4. The pictures of the simulation results shown in Figure 4.11 shows the water droplets at their equilibrium state where the shape is constant.

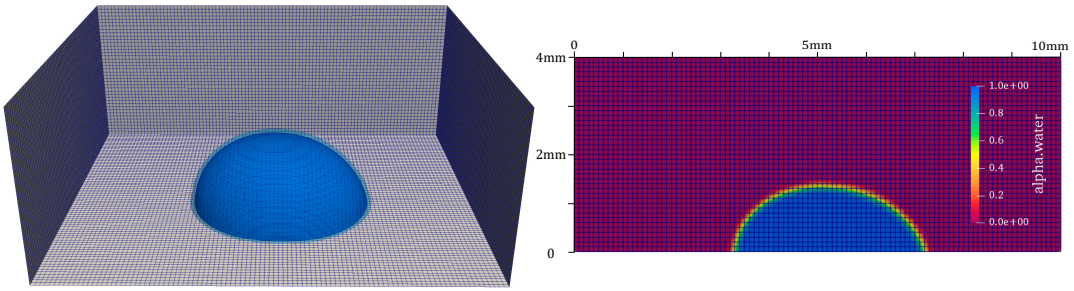

(a) 15µL water droplet on a 20°inclined solid surface.

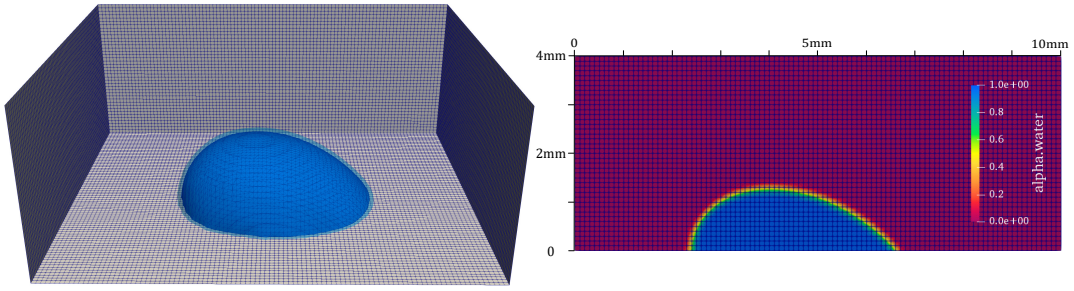

(b) 15µL water droplet on a 60°inclined solid surface.

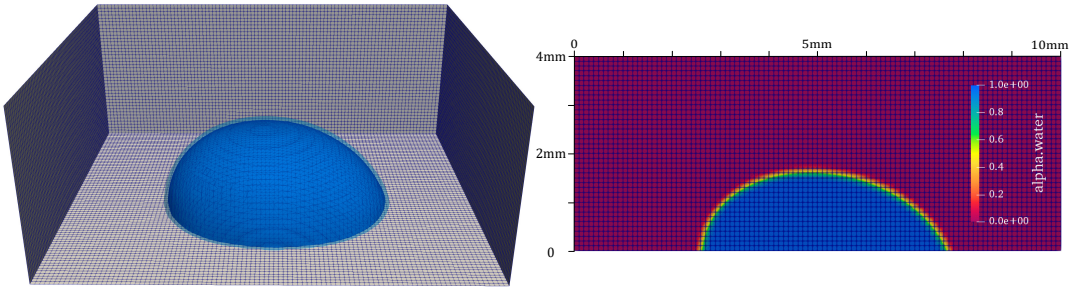

(c) 25µL water droplet on a 20°inclined solid surface.

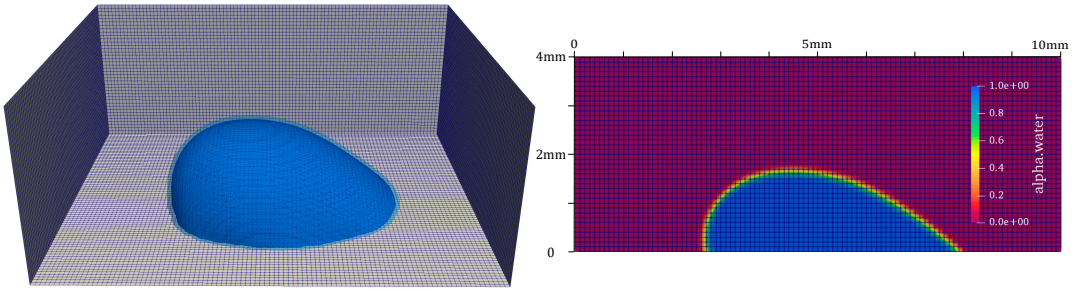

(d) 25µL water droplet on a 60°inclined solid surface.

Figure 4.11: Water droplets with varying size on solid surfaces with varying inclination angles. On the left hand side the droplet is represented by interpolated isosurfaces with the dark blue being at $\alpha_{\text{water}} = 0.5$ and the light blue at $\alpha_{\text{water}} = 0.1$. The right hand side shows the α_{water} field values in a slice through the middle of the domain.

To describe the shape of the water droplet Abdullah Al-Sharafi [2020] introduces two dimensionless numbers. A dimensionless length defined as the ratio between the puddle height of the water droplet h as shown in Figure 4.10 and the capillary length $\lambda = \sqrt{\sigma/\rho g}$. To describe the droplet Abdullah Al-Sharafi [2020] uses the Merve Number MN $= \sqrt{2\rho g r^2/3\sigma}$ which is a ratio between the gravitational forces and surface tension forces. In Figure 4.12 the dimensionless droplet height is plotted as a function of Merve Number. The red points is the data provided in Abdullah Al-Sharafi [2020] and the blue points are from the simulation results. In both the CFD simulations presented here and in Abdullah Al-Sharafi [2020] there is only a negligible difference between the droplet height for varying inclination angle of the solid surface. However the shape of the droplets are still noticeable different as the advancing and receding contact angles changes with varying inclination angles. Compared to Abdullah Al-Sharafi [2020] the simulations slightly overpredicts the dimensionless droplet height as shown in Figure 4.12. These variations can be caused by small differences in the physical properties used.

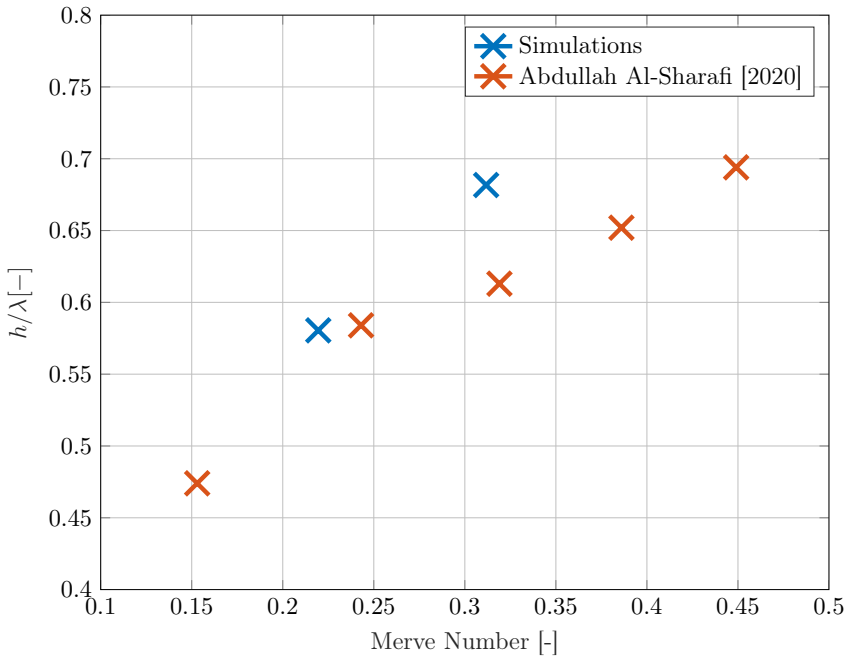

Figure 4.12: Dimensionless droplet height as a function of dimensionless Merve Number for simulations and reference data.

As mentioned previously, the introduction of filling elements into the system will introduce a variety of different inclination angles within the system. As shown is this section the dynamic droplet behaviour on inclined surfaces depends on the droplet size and inclination angle which can not be considered constants in a transient simulation of flow around filling elements. As a results of that it is not possible to define a *dynamicAlphaContactAngle* boundary condition that will be valid for the entire

surface area of the filling elements as both inclination angle and droplet sizes changes throughout the simulation. It is uncertain what impact an accurate model for the advancing and receding contact angles, that considers a varying droplet size and inclination angle for every time step, would have for the overall pressure drop of the system. It is believed that the definition of contact angles in the simulations mostly effect the thickness of the water film and does not have a significant impact on the overall specific pressure loss.

5 | Filling Elements Simulations

In the following chapter a series of simulations of a small section of a simple scrubber is presented using both the **interCyclicFoam** and **interIsoCyclicFoam** model. The outer dimensions of the computational domain is 80mm x 80mm x 80mm with the filling elements being 20mm x 20mm x 20mm boxes positioned evenly within the domain. A more detailed view of the computational setups for the different simulations can be found in Appendix B.5. The system is initialized with 24 water droplets with diameters of 13mm evenly distributed throughout the domain as shown in Figure 5.1 using interpolated isosurfaces. This volume corresponds to 3% of the entire computational domain which is a common water fraction used in sea water scrubbers. All the outer boundaries are defined as periodic pairs whereas as the filling elements are considered walls. The wettability of the filling elements are defined as neutral with a constant contact angle of 90°. As shown in Chapter 4 the contact angles have an effect on the droplet behaviour on the surface, however its impact on the overall flow behavior is believed to be insignificant.
The function *meanVelocityForce* presented in Section 3.1, that controls the gas velocity in counterflow to the water by adding a source term to the momentum equation in each cell, is not utilized for the simulations presented in this chapter. The reason for this exclusion is because of stability issues where the simulations crashed before the simulations finished. The cause for the instabilities is most likely the non-physical way the source term is added to the momentum equation in every cell in the domain. Ideally the source term is only added to the cells that only contains gas, however such an implementation would require both solvers to be rewritten. As a consequence of this the simulations presented in this section does not have the gas and water in counterflow, instead the fluids are in cocurrent in the gravitational direction.
The purpose of the chapter is to investigate the difference between the two models in terms of how well the interphase between the fluids is resolved and how well the water volume is conserved over time. In the simulations the thickness of the interphase between water and gas is visualized by using interpolated isosurface plots at $\alpha_{\text{water}} = 0.5$ and $\alpha_{\text{water}} = 0.1$. In an ideal case there is no differences between these isosurfaces as the interphase is considered a continuous jump. However in numerical simulations using the VOF method this is not possible to obtain. Therefore the difference between the two isosurfaces is used to evaluate how well the interphase is resolved. A small difference in the isosurfaces indicate a thin interphase whereas a large difference means the interphase is poorly resolved.

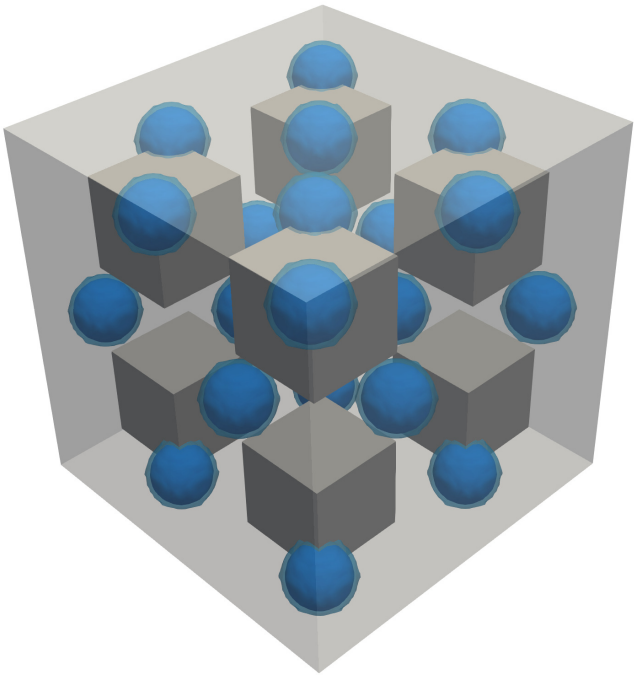

Figure 5.1: The computational setup at $t = 0$. The water is represented as interpolated isosurfaces. The dark blue is at $\alpha_{\text{water}} = 0.5$ and the light blue is at $\alpha_{\text{water}} = 0.1$.

To properly compared the performance and differences between the **interCyclicFoam** and **interIsoCyclicFoam** solver simulations have been conducted on three different mesh refinements all using quadratic hexahedron cells. The cell size and total number of cells for the three simulations is shown in Table 5.1.

Table 5.1: Mesh parameters for the three different simulations.

Simulation	Cell size [mm]	Cell count [-]
Coarse	1	448 000
Medium	0.66	1 512 000
Fine	0.5	3 584 000

The simulation results are shown after 0.5s in Figure 5.2 on the three different mesh refinement for both solvers. For the **interCyclicFoam** simulations is it clear that the interphase is better resolved on the fine grid compared to the coarse and medium grid. On the coarse grid, Figure 5.2a, there are large areas where the water volumetric fraction is between 0.1 and 0.5, shown in the figure as the light blue areas, and only the larger clumps of water have a water volumetric fraction above 0.5 (the dark blue areas). For the fine simulation on the other hand, Figure 5.2e, the difference between the $\alpha_{\text{water}} = 0.5$ and $\alpha_{\text{water}} = 0.1$ isosurface are much smaller indicating that the interphase is better resolved. Most of the smaller water droplets consists of cells with $\alpha_{\text{water}} > 0.5$ which was not the case in the coarse simulation using **interCyclicFoam**.

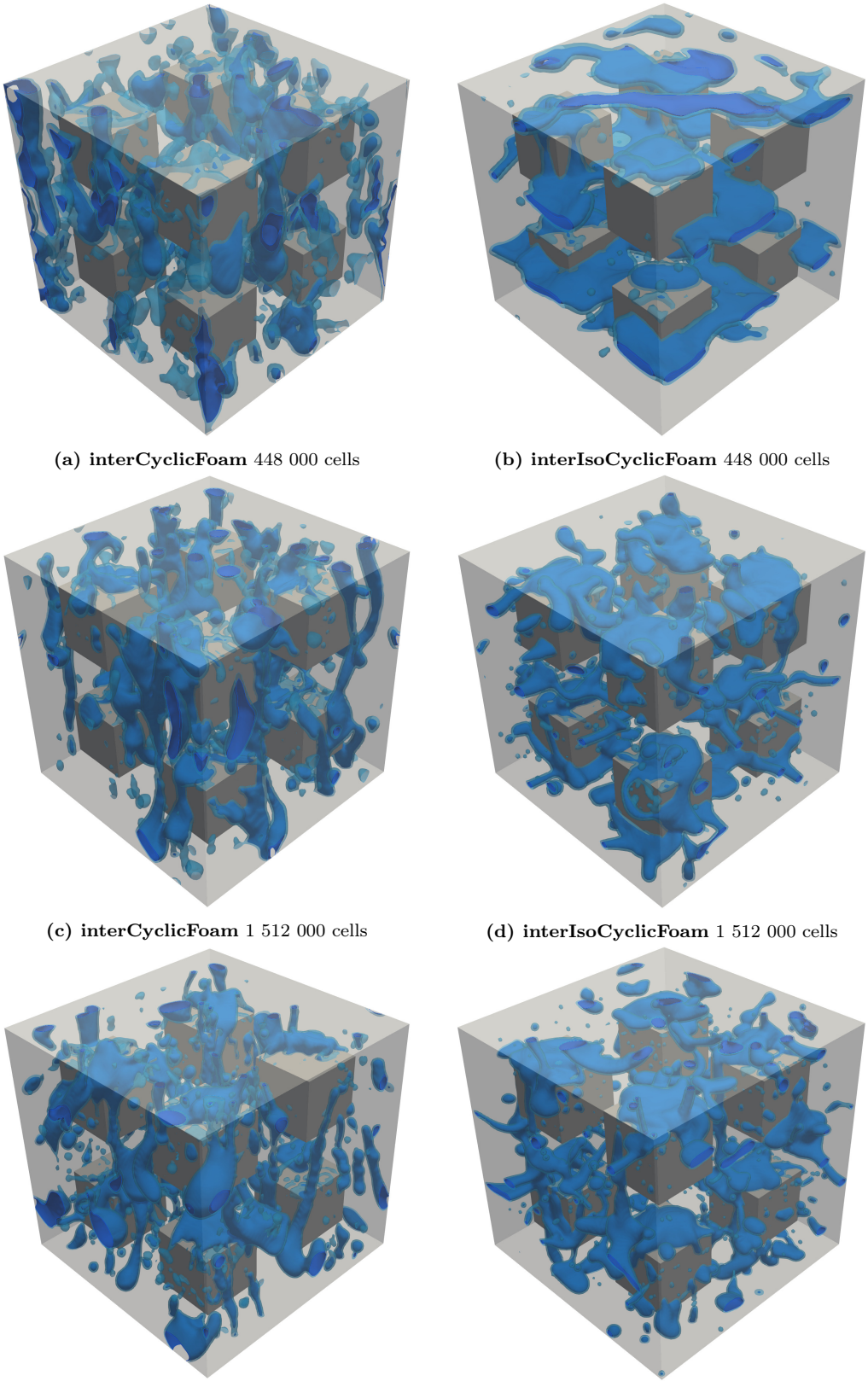

(a) interCyclicFoam 448 000 cells

(b) interIsoCyclicFoam 448 000 cells

(c) interCyclicFoam 1 512 000 cells

(d) interIsoCyclicFoam 1 512 000 cells

(e) interCyclicFoam 3 584 000 cells

(f) interIsoCyclicFoam 3 584 000 cells

Figure 5.2: Simple fill elements simulation results at $t = 0.5$s for both the **interCyclicFoam** and **interIsoCyclicFoam** solver. The water is represented by isosurfaces, the dark blue is at $\alpha_{\text{water}} = 0.5$ and the light blue is at $\alpha_{\text{water}} = 0.1$.

For the simulations using **interIsoCyclicFoam** the differences between the different meshes are not as much in how well the interphase is resolved, but rather to what extent the water splits up into smaller droplets. In the coarse simulation, Figure 5.2b, the interphase is very thin, shown by the difference between the $\alpha_{\text{water}} = 0.5$ and $\alpha_{\text{water}} = 0.1$ isosurface being small. Except for a few small droplets all the water is in larger clumps in the coarse simulation. When the mesh is refined more in Figure 5.2d and 5.2f the water stats to split-up into smaller droplets whilst still maintaining a thin interphase.

As previously mentioned, how well the interphase between the fluids are resolved is defined as the difference between the isosurfaces. In Figure 5.3 the area of the isosurfaces shown in Figure 5.2 are measured, divided by the volume of the domain and plotted for all six simulations. In the coarse simulations using **interCyclicFoam** the area of the $\alpha_{\text{water}} = 0.1$ isosurface is 2.7 times higher than the $\alpha_{\text{water}} = 0.5$ isosurface. For the fine simulation this fraction is reduced to 1.6 indicating a clear improvement is how well the problem is resolved.
For the simulations using **interIsoCyclicFoam** the difference in the effective surface area is almost unchanged. Overall the surface area increases when refining the mesh which is caused by the water splitting up into more smaller droplets. From Figure 5.3 it can be concluded that the **interCyclicFoam** solver obtain results with a more thin and well refined interphase when refining the mesh. For the **interIsoCyclicFoam** solver on the other hand there is no significant improvements in the refinement of the interphase when improving the mesh. The **interIsoCyclicFoam** solver does however has a much more well refined interphase on coarse meshes than the **interCyclicFoam** solver.

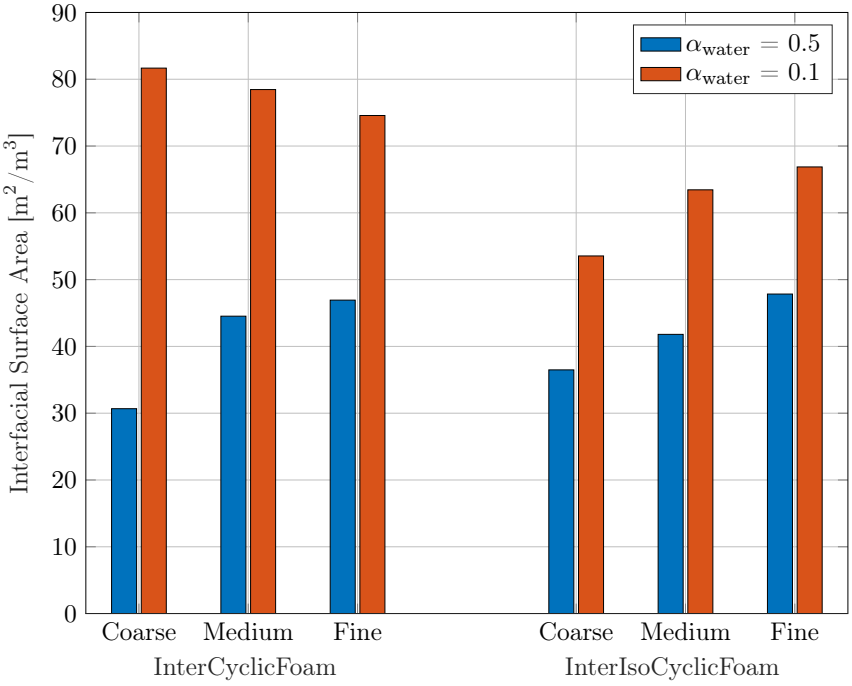

Figure 5.3: The specific interfacial area between water and gas.

Another important performance parameter is the conservation of the water volume over time. In Figure 5.4 the relative water volume is plotted as a function of time for all six simulations. The difference in starting volume is due to the selection of cells. In the computational setup 24 spheres with a diameter of 13mm are initialized with $\alpha_{\text{water}} = 1$, however the volume of the cells within these spheres varies for the different mesh refinements. In Figure 5.4 the water volume plotted is relative to the fine mesh and the coarser meshes starts at a slightly lower water volume.
As shown in Figure 5.4 the water volume is completely conserved in the **interCyclicFoam** simulations, however for the **interIsoCyclicFoam** simulations the water volume decreases over time. The relative amount of water lost decreases when refining the mesh, with the fine simulations losing 5% and the coarse losing 12%. In Section 3.2 it was mentioned that the **interIsoCyclicFoam** solver seems to lose a small amount of water each time it passes through the periodic boundaries. This can also be the case in the simulations presented here as the even distribution of water in the domain makes is so that there is always water passing through the periodic boundaries and the total water volume steadily deceases as a result of that.

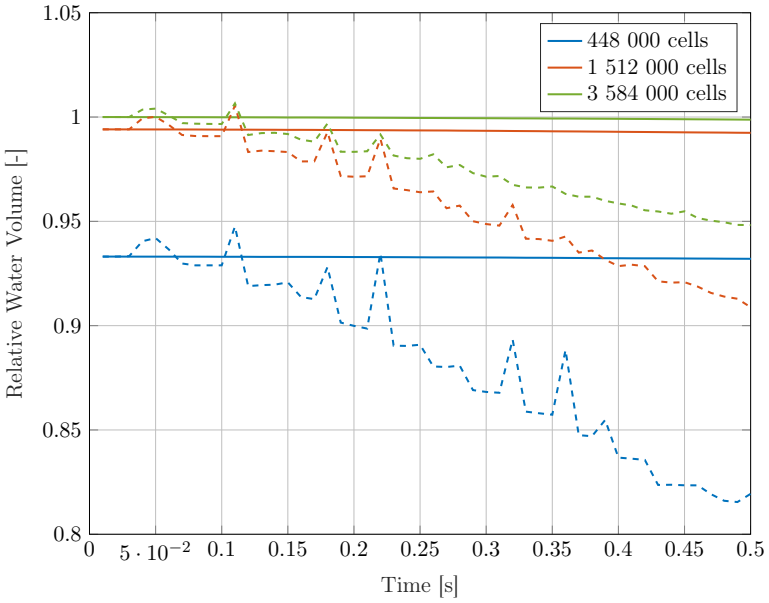

Figure 5.4: Relative water volume as a function of time. The solid curves are from the model **interCyclicFoam** and the dashed curves are from **interIsoCyclicFoam**.

Bases on the simulations presented in this chapter it can be concluded that the **interIsoCyclicFoam** is not suited for simulations of the two-phase flow behaviour in the scrubber absorption column. Even though the model recreates a sharp intherphase between the two fluids on coarse meshes, which can drastically reduces the calculation time, the issues with the water volume conservation is a major problem. For the simulations to be useful is the design of scrubbers it is required that the simulation can run long enough to reach a steady performance in terms of pressure loss. During that time it is important the interphase between the fluids remains sharp and that the water is conserved within the system, where the latter does not seem to be obtainable with the **interIsoCyclicFoam** solver.
For the **interCyclicFoam** solver there is no issues with the conservation of water for any of the three meshes presented here, however to obtain a sharp interphase between the fluids a very fine mesh is required. This means that the **interCyclicFoam** solver should be able to obtain a steady preformance solution with a sharp interphase and conservation of water, but it will be computationally very expensive.

6 | Conclusion

The present study numerically investigates the flow behaviour on and around solid surfaces while using periodic boundary conditions. Transient Reynolds-Averaged Navier-Stokes (RANS) simultions are performed using the Volume of Fluid method. The performance of two different VOF models, **interCyclicFoam** and **interIsoCyclicFoam**, were investigated with the difference being in the scheme used to calculate the interphase between the two fluids. The computational domains used throughout the report is very small, compared to the size of the absorption column in a scrubber, and should only represent a small section of the column.

Two different validations were conducted to investigate the performance of using periodic boundary conditions. The first was of the pressure loss in a duct of a single phase. Here it was found that when using a small domain with periodic boundary condition in inlet/outlet the highest deviation from the analytical solution was 6.25% at 6m/s. At 3m/s, which is approximately the gas velocity in a seawater scrubber, there was no noticeable difference between the analytical and the simulation results. The second validation was of the terminal velocity of a water droplet. The simulation results were compared to an analytical solution that uses the force balance to predict the terminal velocity of the droplet. The **interCyclicFoam** solver under predicted the analytical terminal velocity by 22% whereas the **interIsoCyclicFoam** solver over predicted it by 17%. The validation also showed a significant improvement in performance when refining the mesh, indicating that a fine mesh is required in order to obtain accurate results.

The waters interaction with solid surfaces were investigated though a series of simulations. Based on the results it can be concluded that a high wettablity on the solid surface, represented by a low contact angle θ, leads to the droplet occupying a larger area on the solid surface which leads to a thin film layer. Furthermore the shape of a water droplet at rest on a solid surface can be considered as a spherical cap at $\mathrm{Bo} < 1$. The dynamic behavior of a water droplet hitting a solid surface was investigated and the simulation results showed a spreading diameter well within the range of the four empirical correlations from other studies. Finally the dynamic behaviour of water droplets moving along an inclined solid surface was investigated. It was found that the dynamic contact angles depends on the inclination angle and droplet size. In the simulations the shape of the droplets were different for varying inclination angles, however the droplet height were almost constant. This is in agreement with the experimental data found in other studies.

The performance of the two models, **interCyclicFoam** and **interIsoCyclicFoam** was investigated on a small simplified section of a scrubber absorption column. The results for the **interIsoCyclicFoam** solver showed that the interphase between the two fluids was well refined even for coarse meshes, however the water volume was not

conserved over time. The **interCyclicFoam** solver on the other hand did conserve the water volume, but how well the interphase was resolved heavily depended on the refinement of the mesh. Based on these observations it can be concluded that the **interIsoCyclicFoam** solver is not suited for the complex multiphase flow phenomena occurring inside a scrubber due to the inability to conserved the water volume. The **interCyclicFoam** solver is more suited as it does not have the same problem, however a fine mesh is required to properly resolve the interphase and thereby the simulations will be computationally expensive.

The filling element simulations done in this study were conducted on a simple geometry compared to an actual packed bed scrubber column and the results are therefor not directly applicable to the design of a scrubber. However the **interCyclicFoam** model developed in this study can be expanded to simulations of the actual packed bed geometry of a scrubber and be used to predict the the specific pressure loss and the interfacial area between the the fluid phases. To optimize the performance of the scrubber system, the interfacial area should be sufficiently high to remove the sulphur content while keeping the pressure loss at a minimum. The model can be used to test different design parameters like the filling elements or the water load.

Bibliography

Abdullah Al-Sharafi, **2020**. Haider Ali H. Al-Qahtani Abdullah Al-Sharafi, Bekir S. Yilbas. *Adhesion of a water droplet on inclined hydrophilic surface and internal fluidity*. International Journal of Adhesion Adhesives, 96(1), 2020. doi: https://doi.org/10.1016/j.ijadhadh.2019.102464.

Ali Majid, **2012**. Sun Zhongning Wang Jianjun Gu Haifeng Ali Majid, Yan Changqi. *CFD simulation of dust particle removal efficiency of a venturi scrubber in CFX*. Nuclear Engineering and Design, 256(1), 2012. doi: http://dx.doi.org/10.1016/j.nucengdes.2012.12.013.

Andraž Pavlišič, **2018**. Andrej Pohar Blaž Likozar Andraž Pavlišič, Rok Ceglar. *Comparison of computational fluid dynamics (CFD) and pressure drop correlations in laminar flow regime for packed bed reactors and columns*. Powder Technology, 328(1), 2018. doi: https://doi.org/10.1016/j.powtec.2018.01.029.

Ansys, **2009**. Ansys. *Ansys Fluent 12 Theory Guide*. `https://www.afs.enea.it/project/neptunius/docs/fluent/html/th/main_pre.htm`, 2009.

C. Béguin, **2017**. M.J. Pettigrew C. Béguin, S. Étienne. *Effect of dispersed phase fraction on the drag coefficient of a droplet or a bubble in an idealized two-phase flow*. European Journal of Mechanics / B Fluids, 65(1), 2017. doi: http://dx.doi.org/10.1016/j.euromechflu.2017.05.009.

Cengel Y, **2012**. Turner R Cengel Y, Cimbala J. *Fundamnentals of Thermal-Fluid Sciences*. McGraw-Hill Education, 4 edition, 2012.

F. Menter, **2003**. T. Esch B. Konno F. Menter, J. C. Ferreira. *The SST Turbulence Model with Improved Wall Treatment for Heat Transfer Predictions in Gas Turbines*. International Gas Turbine Congress, 1(1), 2003.

Guoli Li, **2020**. Xiongwen Xu Xingbin Lu Jianxun Chen Guoli Li, Jinping Liu. *Contact angle measurements in the refrigerant falling film evaporation process*. International Journal of Refrigeration, 112(1), 2020. doi: https://doi.org/10.1016/j.ijrefrig.2019.12.017.

Ilkers Bayer, **2006**. Constantine Megaridis Ilkers Bayer. *Contact angle dynamics in droplets impacting on flat surfaces with different wetting characteristics*. Journal of Fluid Mechanics, 558(1), 2006. doi: https://doi.org/10.1017/S0022112006000231.

IMO, **2018**. International Maritime Organization IMO. *Sulphur oxides (SOx) and Particulate Matter (PM) – Regulation 14*. `http://www.imo.org/en/OurWork/Environment/PollutionPrevention/AirPollution/Pages/Sulphur-oxides-(SOx)-%E2%80%93-Regulation-14.aspx`, 2018. Downloaded 2020-05-28.

Ion Iliuta, **2019**. Maria C. Iliuta Ion Iliuta. *Modeling of SO2 seawater scrubbing in countercurrent packed-bed columns with high performance packings*. Separation and Purification Technology, 226(1), 2019. doi: https://doi.org/10.1016/j.seppur.2019.05.078.

Jia-Meng Tian, **2019**. Bin Chen Jia-Meng Tian. *Dynamic behavior of non-evaporative droplet impact on a solid surface: Comparative study of R113, water, ethanol and acetone*. Experimental Thermal and Fluid Science, 105(1), 2019. doi: https://doi.org/10.1016/j.expthermflusci.2019.03.024.

Alfa Laval. Pure SOx. `https://www.alfalaval.com/products/process-solutions/scrubber-solutions/exhaust-gas-cleaning/puresox/`, 2019. Downloaded: 2020-05-28.

Manisha Bal, **2017**. Bhim Charan Meikap Manisha Bal. *Prediction of hydrodynamic characteristics of a venturi scrubber by using CFD simulation*. South African Journal of Chemical Engineering, 24(1), 2017. doi: https://doi.org/10.1016/j.sajce.2017.10.006.

M.W. Baltussen, **2014**. N.G. Deen M.W. Baltussen, J.A.M Kuipers. *A critical comparison of surface tension models for thevolume offluid method*. Chemical Engineering Science, 109(1), 2014. doi: http://dx.doi.org/10.1016/j.ces.2013.12.045.

Nichols, **1979**. C. W. Hirt B. D. Nichols. *Volume of Fluid (VOF) Method for the Dynamics of Free Boundaries*. Los Alamos Scientific Laboratory, 1(-), 1979.

OpenFOAMWiki, **2018**. OpenFOAMWiki. *InterFoam*. `https://openfoamwiki.net/index.php/InterFoam`, 2018. Downloaded 2020-05-28.

Roenby J, **2017**. Bredmose H Jasak H. Roenby J, Larsen B. *A NEW VOLUME-OF-FLUID METHOD IN OPENFOAM*. VII International Conference on Computational Methods in Marine Engineering, 1(1), 2017.

Roenby J, **2016**. Jasak H. Roenby J, Bredmose H. *A computational method for sharp interface advection*. Royal Society Open Science, 1(1), 2016. doi: http://dx.doi.org/10.1098/rsos.160405.

Roisman, **2009**. Ilia V. Roisman. *Inertia dominated drop collisions. II. An analytical solution of the Navire-Stokes equations for a spreading viscous film*. Physics of Fluids, 21(052104), 2009. doi: DOI:10.1063/1.3129283.

Anders S Simonsen. Modelling and analysis of seawater scrubber for reducing SOx emissions from marine engines. PhD thesis, Aalborg University, 2018.

WHO, **2016**. World Health Organization WHO. *Ambient air pollution: A global assessment of exposure and burden of disease*. WHO Library Cataloguing-in-Publication Data, 1 edition, 2016.

Yukihiro Yonemoto, **2020**. Tomoaki Kunugi Yukihiro Yonemoto. *Estimating critical surface tension from droplet spreading area*. Physics Letters, A(384), 2020. doi: https://doi.org/10.1016/j.physleta.2019.126218.

A | OpenFOAM Solver Setup

Is this appendix, the OpenFOAM setup is presented. It includes the physical properties used throughout all simulations, the numerical schemes and the solver settings. Not all of the listed parameters have been testes in this study and the information listed in the following is what yielded stable solutions and is not fully optimized in terms of calculation speed.

A.1 Physical Properties

The physical properties used for the two fluids water and gas are listed in Table A.1. These are considered as constants in all the simulations presented throughout the study.

Table A.1: A list of physical properties used throughout all simulations.

Parameter	Symbol	Value	Units
Gravitation	g	9.82	$\mathrm{m/s^2}$
Surface Tension	σ	0.07	N/m
Density	ρ_w	1000	$\mathrm{kg/m^3}$
	ρ_a	1	$\mathrm{kg/m^3}$
Kinematic Viscosity	ν_w	10^{-6}	$\mathrm{m^2/s}$
	ν_a	$1.48\,10^{-5}$	$\mathrm{m^2/s}$

A.2 Numerical Schemes

To solve the governing differential equations, they are discretized over the domain and a number of different numerical schemes are then required specified in the model. The schemes used for this study is listed in Table A.2 and includes time derivatives $\frac{\partial}{\partial t}$, gradients ∇U, divergence terms $\nabla\left(\bar{u}_\mathrm{i}\bar{u}_\mathrm{j}\right)$ and laplacian terms ∇^2. Furthermore the interpolation from cell-center to face-center is computed using interpolation schemes and the surface normal gradient is computed with the snGradSchemes. Not all the schemes are bounded and it is therefore important to make sure that the final solution is physically possible for every timestep.

Table A.2: The different schemes used in the OpenFOAM simulation.

Category	**Term**	**Scheme**	$\mathcal{O}(h^n)$	**Bounded**
ddtScheme	default	Euler	1st	No
gradScheme	default	Gauss linear	2nd	No
	grad(U)	CellLimited Gauss linear 1	2nd	Yes
divSchemes	div(rhoPhi,U)	Gauss linearUpwind grad(U)	2nd	Yes
	div(phi,alpha)	Gauss vanLeer	2nd	No
	div(phirb,alpha)	Gauss linear	2nd	No
	div(((rho*nuEff)* dev2(T(grad(U)))))	Gauss linear	2nd	No
	div(phi,omega)	Gauss limitedLinear 1	2nd	No
	div(phi,k)	Gauss limitedLinear 1	2nd	No
laplacianSchemes	default	Gauss linear limited corrected 0.33	2nd	No
interpolation-Schemes	default	linear	2nd	No
snGradSchemes	default	limited corrected 0.33	2nd	No

A.3 Solver Settings

In addition the the numerical schemes a number of solver settings are also specified for the different fields. This include the solver, preconditioner and tollerance as listed in Table A.3. The maximum number of iteration is by default 1000 in OpenFOAM.

Table A.3: Solvers, tolerances and operating conditions for the different fields used in the OpenFOAM simulation.

Fields	**Solver**	**relTol**	**Tolerance**	**Precon-ditioner**	**Smoother**
alpha.water	smoothSolver	0	$1 \cdot 10^{-8}$	-	symGaussSeidel
p_{rgh}	PCG	0.05	$1 \cdot 10^{-8}$	DIC	-
$p_{rghFinal}$	PCG	0	$1 \cdot 10^{-8}$	DIC	-
U	smoothSolver	0	$1 \cdot 10^{-6}$	-	SymGaussSeidel
(k|omega)	smoothSolver	0.1	$1 \cdot 10^{-6}$	-	GaussSeidel
(k|omega)Final	PBiCG	0	$1 \cdot 10^{-6}$	DILU	-

B | Simulation Computational Setup

In this appendix the OpenFOAM computational setup is described in more detail for the simulations made throughout the report. It includes the meshing, boundary conditions and initial state at $t = 0$.

B.1 Duct Specific Pressure Loss Simulations

For the transient simulations of the specific pressure loss in a duct using **interCyclicFoam** the computational domain is a quadratic 50mm x 50mm x 50mm box as shown in Figure B.1. The cells all hexahedrons and are evenly distributed in the entire domain with the cell size 0.66mm x 2mm x 0.66mm which results in the total cell count being 140 625. The inital sate is the domain filled with air with $U = (0\,0\,0)$.

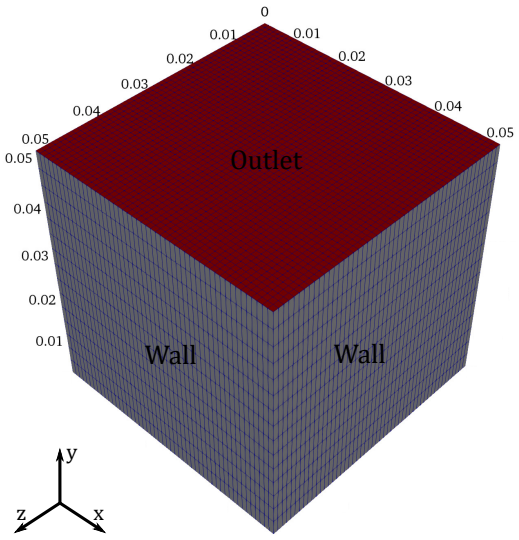

Figure B.1: Computational domain for the transient duct simulations.

The boundary conditions is a periodic pair between the inlet and outlet (bottom and top) and wall boundary conditions on the sides of the domain. The implemented boundary conditions in OpenFOAM is shown in Table B.1.

Table B.1: A list of boundary conditions for the transient simulations using periodic boundary conditions and the solver **interIsoCyclicFoam**.

Patch	U	P	α_{water}
Wall	no-slip	zeroGradient	zeroGradient
Inlet	cyclic	cyclic	cyclic
Outlet	cyclic	cyclic	cyclic

For the steady state simulations of the specific pressure loss is a duct using **simpleFoam** the domain is the entire 50mm x 20m x 50mm duct. The cells size is 1mm x 100mm x 1mm with the total number of cells being 500 000. The boundary conditions is a uniform inflow in the inlet patch and a fixed pressure at the outlet while having wall boundary conditions on the sides. The full list of boundary conditions is shown in Table B.2.

Table B.2: A list of boundary conditions for the steady state simulations using **simpleFoam** as the solver.

Patch	U	P
Wall	no-slip	zeroGradient
Inlet	fixedValue (0 U_y 0)	zeroGradient
Outlet	zeroGradient	fixedValue 0

B.2 Terminal Velocity Simulations

For the transient simulations using both the **interCyclicFoam** and **interIsoCyclicFoam** solver the computational domain is a 25mm x 25mm x 25mm quadratic box as shown in Figure B.2. Hexahedron cells are evenly distributed in the domain with the initial size 0.5mm x 0.5mm x 0.5mm. During the simulations the mesh is further refined in the interphase between water and gas using the utility *dynamicMeshRefine*. This refines the cells in the boundary to 0.125mm x 0.125mm x 0.125mm or 0.0625mm x 0.0625mm x 0.0625mm in the fine case. The initial state is a water droplet with a diameter of 1mm in the center of the domain and $U = (0\,0\,0)$ for every cell. Due to the selection of cells the resulting water droplet has a diameter of 1.2mm.

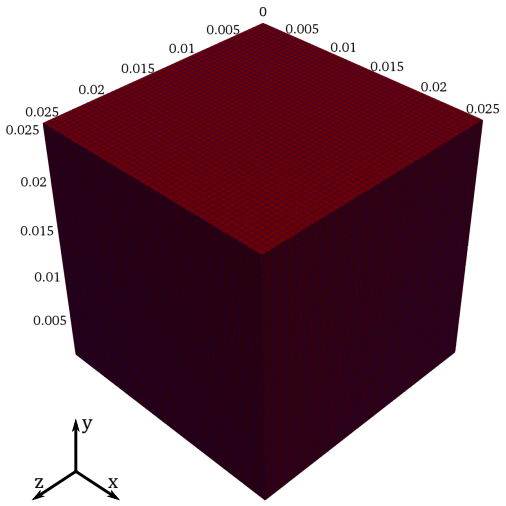

Figure B.2: Computational domain for the terminal velocity simulations.

The simulations uses the turbulence model k-ω-SST, *Shear Stress Transport* [F. Menter, 2003]. The boundary conditions for all fields are periodic/cyclic as shown in Table B.3 with the pairs being the inlet/outlet, left/right and front/back.

Table B.3: A list of boundary conditions for the transient simulations of a droplet falling using periodic boundary conditions.

Patch	U	P	α_{water}	k_{t}	ω_{t}
Wall	cyclic	cyclic	cyclic	cyclic	cyclic
Inlet	cyclic	cyclic	cyclic	cyclic	cyclic
Outlet	cyclic	cyclic	cyclic	cyclic	cyclic

B.3 Contact Angle Simulations

The same computational setup is used for the simulations of difference surface wettability in Section 4.1 and the spreading factor in Section 4.2. The outer domain is a flat box with varying size depending on the droplet size. The dimensions of the box is $5D$ x $2D$ x $5D$ where D is the diameter of the water droplet. In Figure B.3 an example of the computational domain is shown for a water droplet with a diameter of 2mm. The domain initially contains 50 000 hexahedron cells and the utility *dynamicRefineMesh* is used to refine the cells in the interphase between the two fluids.

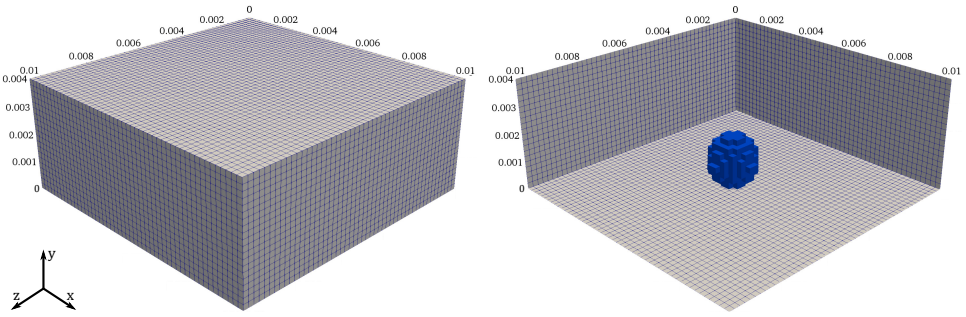

Figure B.3: The computational domain for a water droplet with diameter 2mm. The blue sphere is the cells initialized with $\alpha_{\text{water}} = 1$ at $t = 0$.

In Table B.4 the boundary conditions are listed. The bottom patch is where the water-solid interaction is occurring and the *constantAlphaContactAngle* is used to specify the contact angle on the boundary.

Table B.4: A list of boundary conditions for the transient simulations of varying contact angles and the spreading factor using **interCyclicFoam** as the solver.

Patch	U	P	α_{water}
Wall	no-slip	zeroGradient	zeroGradient
Bottom	no-slip	zeroGradient	constantAlphaContactAngle θ
Top	pressureInletOutletVelocity	fixedValue 0	inletOutlet

B.4 Dynamic Contact Angle Simulations

The domain used for the dynamic water droplet behaviour is shown in Figure B.4. The outer dimensions of the domain is 10mm x 4mm x 8mm and the total number of cells is 320 000 with a cell size of 0.1mm x 0.1mm x 0.1mm. The inclination angle of the domain is controlled by varying the angle is which the gravitational force is acting. A spherical water droplet is initialized as shown on the right in Figure B.4 and the velocity is $U = (0\,0\,0)$ at $t = 0$.

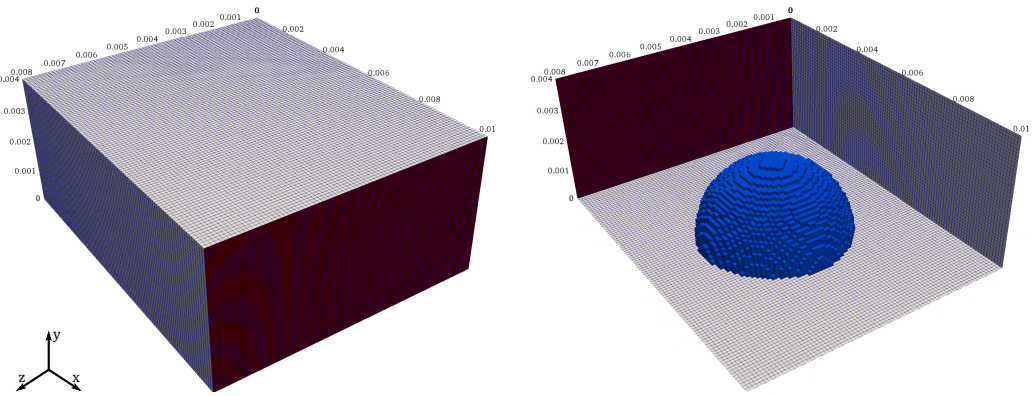

Figure B.4: The computational domain for dynamic droplet behaviour. The blue sphere is the cells initialized with $\alpha_{\text{water}} = 1$ at $t = 0$.

During the simulation the droplet is moving in the x-direction between the periodic boundaries indicated as the red patches. The rest of the patched are considered walls and uses the *dynamicAlphaContactAngle* to specify the receding and advancing contact angles according to Abdullah Al-Sharafi [2020]. Table B.5 shows the full list of the boundaries used for the simulations.

Table B.5: A list of boundary conditions for the transient simulations of varying inclination angle and droplet size using the **interCyclicFoam** solver.

Patch	U	P	α_{water}
Wall	no-slip	zeroGradient	dynamicAlphaContactAngle $\theta = 130$
Inlet/Outlet	cyclic	cyclic	cyclic

B.5 Filling Element Simulations

The filling elements simulations are conducted on a small 80mm x 80mm x 80mm domain as shown in Figure B.5 which should represent a small section of an absorption column. The filling elements in the simulations are eight 20mm x 20mm x 20mm boxes within the domain. The elements are positioned evenly in the domain with half the distance to the side walls. This means the all outer boundaries can be seen a symmetry planes when the periodic boundaries are applied. A total of 24 water droplets are initialized within the domain, shown as the blue spheres in Figure B.5. The velocity at $t = 0$ is $U = (0\,0\,0)$ for all cells in the domain.

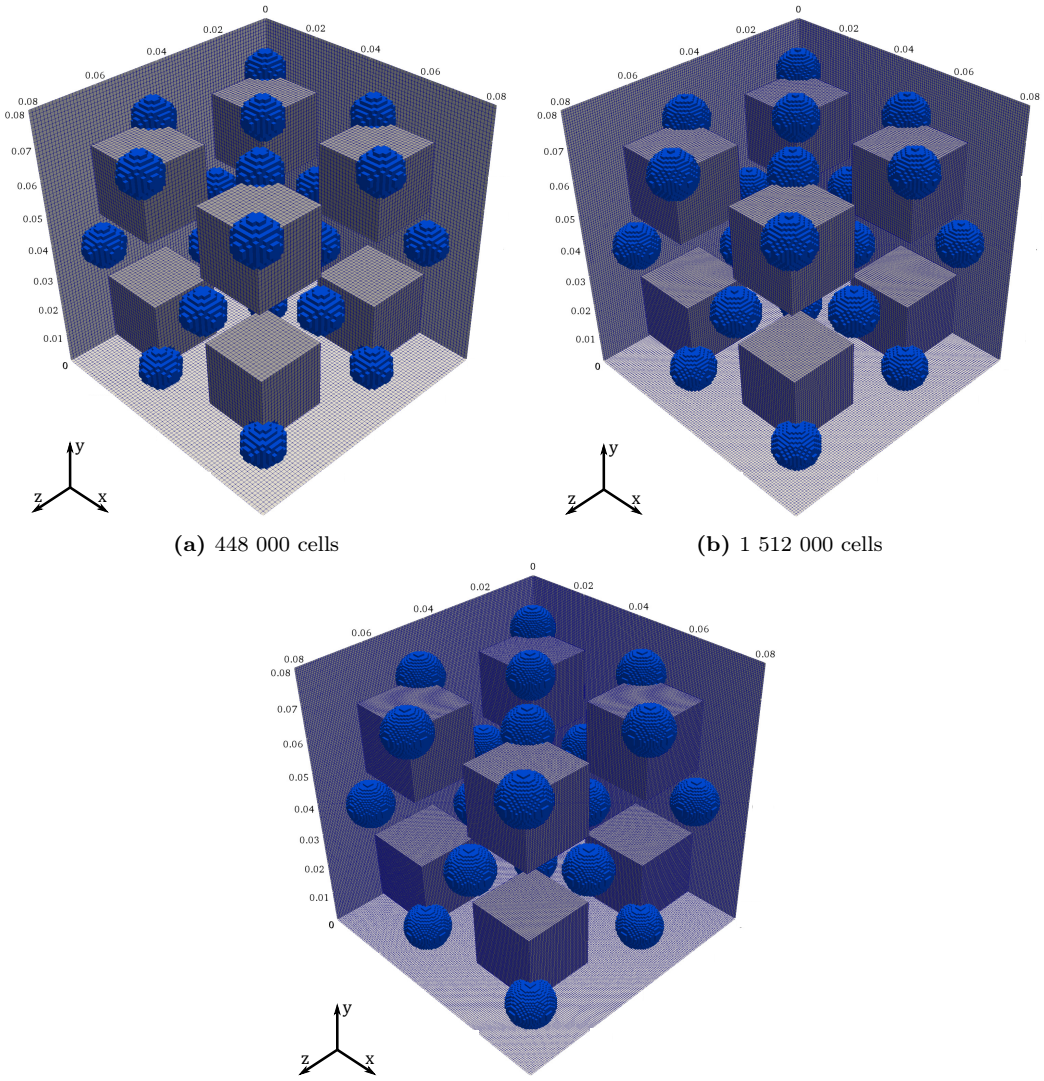

(a) 448 000 cells

(b) 1 512 000 cells

(c) 3 484 000 cells

Figure B.5: Computational domains for the fill elements simulations.

A list of the boundary conditions used for the simulations is shown in Table B.6. All the outer boundaries are periodic pairs and the filling elements are considered walls with no-slip condition. In the simulations the turbulence is modelled using the k-ω-STT model and low Reynolds number wall functions. These are active and compute the boundary when the $y+$ value exceeds unity, however if the $y+$ value is below unity the boundary layer are resolved normally.

Table B.6: A list of boundary conditions for the transient simulations of a small domain with filling elements using periodic boundary conditions.

Patch	U	P	α_{water}	k_{t}	ω_{t}
Sides	cyclic	cyclic	cyclic	cyclic	cyclic
Fill	no-slip	zeroGradient	constantAlpha-ContactAngle $\theta = 90$	kLowReWall-Function	omegaWall-Function